

1 **Cell-type-specific characterization of miRNA gene dynamics in immune cell subpopulations**
2 **during aging and atherosclerosis disease development at single-cell resolution**

3 Ana Hernández de Sande¹, Tanja Turunen¹, Maria Bouvy-Liivrand^{1,2}, Tiit Örd³, Senthil Palani⁴, Celia
4 Tundidor-Centeno¹, Heidi Liljenbäck^{4,5}, Jenni Virta⁴, Olli-Pekka Smålander², Lasse Sinkkonen⁶,
5 Thomas Sauter⁶, Anne Roivainen^{4,5,7}, Tapio Lönnberg^{7,8}, Minna U Kaikkonen³ and Merja Heinäniemi¹

6 ¹ School of Medicine, University of Eastern Finland, Kuopio, North-Savo 70200, Finland

7 ² Department of Chemistry and Biotechnology, Tallinn University of Technology, Tallinn 12616, Estonia

8 ³ A. I. Virtanen Institute, University of Eastern Finland, Kuopio, North-Savo 70200, Finland

9 ⁴ Turku PET Centre, University of Turku and Turku University Hospital, FI-20520 Turku, Finland

10 ⁵ Turku Center for Disease Modeling, University of Turku, FI-20520 Turku, Finland

11 ⁶ Department of Life Science and Medicine (DLSM), University of Luxembourg, 4367 Belvaux, Luxembourg

12 ⁷ InFLAMES Research Flagship Center, University of Turku, FI-20520 Turku, Finland

13 ⁸ Turku Bioscience Centre, University of Turku and Åbo Akademi University, FI-20520 Turku, Finland

14

15 * To whom correspondence should be addressed. Merja Heinäniemi Tel: +358 403 553 842; Email:
16 merja.heinaniemi@uef.fi.

17 **ABSTRACT**

18 MicroRNAs (miRNAs) are a class of regulatory non-coding RNAs that finetune cellular functions by
19 modulating the stability and abundance of their target mRNAs, thereby contributing to regulation of
20 tissue homeostasis. miRNA genes are transcribed similarly to protein-coding genes and recent studies
21 have enabled their annotation and quantification genome-wide from bulk nascent transcriptomes. Here,
22 we developed an approach to quantify and integrate miRNA gene signatures into single-cell studies.
23 To characterize miRNA gene expression dynamics, we first compared the suitability of droplet and
24 plate-based single-cell RNA-sequencing (scRNA-seq) platforms using the matched datasets provided
25 by the Tabula Muris Senis and Tabula Sapiens consortiums. We found high concordance between the
26 platforms and with cell type-specific bulk expression data. Based on the comprehensive aging profiles,
27 our analysis comparing spleen immune cells between young and old mice revealed a concordant
28 regulation of miRNAs involved in senescence and inflammatory pathways in multiple immune cell types,
29 including up-regulation of mmu-mir-146a, mmu-mir-101a and mmu-mir-30 family genes. To study the
30 aberrant regulation of immune cell homeostasis and tissue inflammation that pre-dispose to aging-
31 related disease development, we collected transcriptome profiles from atherosclerosis development in
32 LDLR^{-/-}ApoB^{100/100} mice. We found an elevated myeloid cell proportion in the adipose tissue and further
33 characterized the cell subtypes based on reproducible transcriptome clusters. We then compared
34 miRNA gene expression in early versus late disease and upon inflammatory challenge to monitor
35 different stages during disease progression. At atherosclerotic stage, pro-inflammatory mmu-mir-511
36 expression increased in several macrophage subtypes, while immunosuppressive mmu-mir-23b~mir-
37 24-2~mir-27b up-regulation was specific to Trem2⁺ lipid-associated macrophages. The infiltrating
38 monocytes up-regulated mmu-mir-1938 and mmu-mir-22 expression and in classical monocytes
39 maturation further increased mmu-mir-221~222, mmu-mir-511 and mmu-mir-155 expression. To
40 validate that these changes detected from single cell profiles represent miRNA gene transcriptional
41 regulation, we used nascent transcriptomics data from *ex vivo* macrophage cultures with pro-
42 inflammatory stimulation, confirming both rapid and long-lasting transcriptional activation of the miRNA
43 loci studied. Collectively, our work enables integrating miRNA gene analysis to current single cell
44 genomics pipelines and facilitates characterization of miRNA regulatory networks during aging and
45 disease development.

46

47

48

49 INTRODUCTION

50 The study of single-cell (sc) transcriptomes has revolutionized the field of cell biology, enabling
51 identification of new cell types, cellular states and characterizing cellular transitions across healthy
52 tissues and during disease development ¹. MicroRNAs (miRNAs), a class of regulatory non-coding RNA
53 molecules, can base pair to their target messenger RNA (mRNA), thereby interfering with their
54 translation into proteins. Thus, miRNA-mediated post-transcriptional regulation strongly impacts gene-
55 regulatory networks that modulate cell function via controlling cell homeostasis ². At systems level,
56 control of cell state transitions deteriorates over time, impairing cellular homeostasis and tissue function.
57 This process manifests with low-grade tissue inflammation and constitutes a risk for developing
58 inflammatory-related diseases such as diabetes, atherosclerosis, Alzheimer's disease, and certain
59 cancers (reviewed in ^{3,4}).

60 MiRNA genes correspond to long transcripts called primary miRNAs (pri-miRNA) that are transcribed
61 by RNA polymerase II similarly as protein-coding genes. Subsequently, miRNA transcripts are
62 processed into short transcripts, pre-miRNAs, and further into 20-22 nucleotides (nt) long mature
63 miRNAs. During sample preparation for standard bulk RNA-sequencing, the size selection step
64 excludes the processed miRNA transcripts. Therefore, separate protocols for small RNA sequencing
65 have been developed and represent the most common miRNA profiling method (reviewed in ⁵).
66 Recently, these were adapted to achieve cellular resolution, however the feasibility of sc-small RNA-
67 seq is limited by low throughput ^{6,7}.

68 Presently, the comprehensive gene annotations such as Refseq primarily consist of pre-miRNA
69 coordinates, appropriate for small RNA sequencing data analysis rather than conventional
70 transcriptome sequencing. As the reference annotation is commonly utilized in single-cell studies,
71 quantification of miRNA genes and the analysis of their regulation at cell type resolution is lacking. In
72 consequence, our understanding of how miRNAs integrate into regulatory networks that govern cell
73 state homeostasis is incomplete. Acknowledging that single-cell transcriptomics captures between 17
74 to 23% of unspliced reads ⁸, analysis of pri-miRNA transcripts presents an alternative. In our previous
75 work, we developed a comprehensive miRNA gene annotation approach based on nascent
76 transcriptome (Global-run-on coupled with sequencing, GRO-seq), Cap Analysis of Gene Expression
77 (CAGE) and histone marker data that enabled the quantification of pri-miRNA transcriptional activity in
78 a multitude of bulk genomics studies in cell lines and primary tissue contexts ^{9,10}.

79 Here, we leverage our previous approach annotating miRNA gene coordinates to quantify miRNA genes
80 from single-cell transcriptomes. To discover changes in miRNA gene expression that could impact their
81 central role in control of cellular homeostasis, and thereby contribute to the progressive loss of healthy
82 physiology, we used the comprehensive aging mouse dataset, collected by Tabula Muris Senis (TMS)
83 consortium ¹¹⁻¹³, and novel profiles from an atherosclerosis disease model. We demonstrate how
84 miRNA gene activity is impacted in immune cells by aging and during disease development and provide
85 these datasets and annotations as an openly available resource to facilitate further characterization of
86 miRNA regulatory networks.

87 RESULTS

88 Quantification of miRNA gene expression in single-cell transcriptomes

89 To characterize miRNA gene expression dynamics in single cell transcriptomes collected from mouse
90 tissues, we first followed the approach described in ⁹ to obtain mouse transcript coordinates
91 representing intergenic (transcribed from their own promoter) and intragenic miRNA genes that are co-
92 transcribed from introns of their host genes (see Methods, datasets used are listed in Table S1A). For
93 simplicity, miRNA genes transcribed from alternative transcription start site (TSS) were summarized by
94 gene locus, following the current practice of capturing gene-level expression in single-cell datasets (see
95 Methods, similarly human coordinates were adopted from ⁹). This annotation, which resulted in 233
96 intragenic and 135 intergenic miRNA gene loci (368), corresponding to 990 mature miRNAs for mouse,
97 and 511 and 391 loci, respectively, for human (1896 mature miRNA), was integrated into the GenCode
98 transcript annotations (Fig. 1A, Table S1B-C: miRNA gene coordinates).

99 Next, we retrieved the comprehensive aging mouse dataset, collected by the TMS consortium ^{11–13} to
100 serve as the first benchmark for miRNA gene quantification at cellular resolution across tissues. Single-
101 cell transcriptomes collected by TMS were sequenced with 10x Genomics and Switching Mechanism
102 at the 5' end of RNA Template (Smart)-seq2 technologies (Table S1C-D). While both methods follow a
103 poly-A-based priming strategy, 10x Genomics uses 3'-based quantification whereas Smart-seq2
104 captures reads along the entire transcript ¹⁴. To assess which method could more accurately capture
105 miRNA gene expression dynamics, we quantified read counts from miRNA gene coordinates in splenic
106 cells from 3-month-old mice from both platforms (matching human data was retrieved from Tabula
107 Sapiens ¹⁵). MiRNA gene dynamics were studied based on the ability of each platform (i) to measure
108 miRNA gene expression levels, and (ii) the ability to detect miRNA quantified as 'percentage of
109 expression'.

110 In line with previous research, Smart-seq2 libraries performed worse on detecting different miRNA
111 genes: across cell types, on average 225 miRNA were found with 10x Genomics vs. 66 with Smart-
112 seq2, despite that more reads per miRNA gene detected were captured at the utilized sequencing depth
113 (98 vs. 83 per miRNA detected, Fig. S1, ⁷). Overall, expression profiles across cell types correlated well
114 between the two platforms, with a 0.83 correlation among miRNA gene average expression level
115 genome-wide and 0.87 comparing the percentage of expression.

116 To study the relationship between miRNA genes and their corresponding mature forms in individual
117 transcriptomes, we identified miRNA gene markers (n=6) for the main splenic immune cell populations
118 including mouse B-, T-, and NK-cells using the statistical tests for cluster comparison in the Single-Cell
119 Analysis in Python (SCANPY) pipeline (Fig. 1B, dot plot panels). We then retrieved their corresponding
120 mature forms and quantified their expression from polymerase chain reaction (PCR)-based profiles
121 available from the immune cell atlas (GSE144081 from ¹⁶; Fig. 1B, heatmap right panel). Relative
122 expression levels amongst the platforms, across species and between the gene and corresponding
123 mature forms were concordant for highly expressed genes, exemplified by (mmu)-miR-141 with highest

124 expression in B-cells and mmu-miR-340 with high expression in NK-cells and B-cells in relation to T-
125 cells (Fig. 1B, notice that miRNA loci marked * did not have corresponding human data). Overall, the
126 correlations between the percent of expression or average expression in single-cell analysis and mature
127 miRNA expression were generally weaker (0.44 - 0.47 in all the comparisons). However, as the mature
128 miRNA levels are also affected by transcript processing and stability, we performed a more direct
129 benchmark comparison to primary transcription assayed using bulk GRO-seq and parallel 10x
130 Genomics scRNA-seq in the mouse stromal cell line ST2 (see Methods, Fig. 1C). MiRNA genes were
131 divided into 10 bins based on their expression in each sequencing technology (plotted from low to high
132 values in Fig. 1C, light purple indicates 10x Genomics-based scRNA-seq and dark purple GRO-seq
133 signal). Independently of the data type used to bin miRNA genes, the detected expression level was
134 highly comparable at bins of high expression (bins from 6 to 10), whereas the bins corresponding to
135 lower expression levels displayed higher variability. This observation agrees with limitations in efficient
136 capture of low-expressed transcripts in 10x Genomics scRNA-seq datasets ⁷. Taken together,
137 quantifying miRNA gene expression based on 10x Genomics and Smart-seq2 scRNA-seq platforms
138 has high concordance with cell-specific bulk expression data. Since more miRNA genes were detected
139 from 10x Genomics-based profiles, we continued with this technology in downstream analyses to
140 capture miRNA transcription at cellular resolution.

141 **Ageing profiles in splenic immune cells reveal coordinated and cell-type-specific changes in** 142 **miRNA gene expression**

143 During aging, the immune system deteriorates, manifesting in loss of homeostatic mechanisms
144 controlling immune responses that can underlie chronic inflammation and thereby risk for developing
145 various aging-related disease. To gain insights into miRNA expression profiles in aging immune cell
146 subpopulations, we retrieved mouse samples from the TMS consortium, the largest resource of single-
147 cell datasets to study aging in multiple tissues. We focused on the splenic male samples that covered
148 the broadest range of time points. The annotation contained seven major splenic cell types that cluster
149 together independently of the mice age (Fig. 2A and Fig. S2A). During aging, mature NK-cell, T-cells,
150 and plasma cells proportions increased whereas macrophage, proerythroblast, T-cell, and NK-cell
151 proportions decreased (Fig. 2B and Fig. S2B), in line with previous results ¹⁷. Next, we compared within
152 each cell type young (1 and 3 months) and old mice (24 and 30 months) to track progressive, gradual
153 changes in gene expression that are detectable only after sufficient time ¹³ and distinguished in each
154 cell type changes in the expression level within cells expressing the transcript (DE category) or
155 variations in the percentage of cells expressing a particular gene (DZ category) (see Methods, n=6996
156 cells). In total 131 DZ and 58 DE miRNA genes were identified across the different cell types,
157 summarized in Fig. 2C (Table S2). Next, miRNA genes were ranked based on combined p-values
158 (Fisher's exact test, see Methods) to identify concordant changes amongst the five most abundant
159 immune cell types, which revealed 187 and 42 significant (combined p-value < 0.05) miRNAs in DZ and
160 DE categories, respectively. A subset of 94 top ranked miRNA with log₂ fold change in detection rate
161 >0.5 in two cell types are shown in Fig. 2D (refer to Fig. S2C showing their profile in female samples).

162 Several previously aging-associated miRNAs are among the top ranked upregulated miRNA genes in
163 old mice, including elevated expression of mmu-mir-101a, in agreement with its established role in aging
164 brain tissue¹⁸, and mmu-mir-146a and mmu-mir-147 that regulate NF- κ B and Toll-like receptor (TLR)
165 mediated inflammatory responses and induce pre-mature senescence¹⁹⁻²¹. In our analysis, mmu-mir-
166 146a and mmu-mir-147 were concordantly upregulated in the immune cell types analysed and mmu-
167 mir-101a expression increased most in lymphoid cells (T-cells, B-cells, and NK T-cells) of old mice (Fig.
168 2D, top). Interestingly, female samples comprising young (3 months) and adult mice (18 and 21 months)
169 only showed common upregulation of mmu-mir-147 and decrease of mmu-mir-146a and mmu-mir-101a
170 (Fig. S2C).

171 Further expression changes seen in aged immune cells that may aggravate aging phenotypes include
172 downregulation of mmu-mir-706 (Fig. 2D, bottom) with recognized function as an oxidative stress
173 regulator²², upregulation of mmu-mir-30a~30c-2 and mmu-mir-30b~30d (upregulated in 4/5 cell types)
174 representing members of miR-30 family microRNAs that promote senescence (inhibition of DNA
175 synthesis by targeting B-myb²³), the concordant increase in mmu-mir-705 (regulation of aging-related
176 cell fate bias²⁴) and mmu-mir-691 that may promote chronic inflammation (ulcerative colitis²⁵).

177 Our analysis also identified highly cell type-specific changes, exemplified by a decrease in mmu-mir-
178 455 transcription in myeloid cells in line with aging-protective function in osteoarthritis²⁶ (Fig. 2C, E and
179 Fig. S2D). Similarly, the fraction of cells expressing mmu-mir-511 involved in the regulation of TLR-
180 signalling decreased. In contrast, we observed upregulation of mmu-mir-138-1 and mir-676
181 transcription towards aging in myeloid cells. Previously similar pattern towards aging has been reported
182 in keratinocytes where miR-138 promotes cellular senescence via targeting *Sirt1*²⁷. These myeloid-
183 lineage specific changes matched specific sub-populations of cells, corresponding to dendritic cells and
184 macrophages (refer to Fig. 2F showing the respective marker genes: *H2-DMb1* for antigen presenting
185 dendritic cells and *Cd163* for macrophages).

186 Taken together, our analysis revealed aging-related transcriptional changes of miRNA genes involved
187 in regulatory networks governing senescence, oxidative stress and inflammatory responses,
188 distinguishing several miRNAs impacted in multiple immune cell types and providing the resolution to
189 detect highly cell type-specific expression.

190 **Identification of miRNA gene markers for myeloid subpopulations in fat tissue**

191 An unhealthy diet is a risk factor for disease development that can result in elevated white adipose
192 tissue (WAT) inflammation through altered cytokine and chemokine secretion in which specific immune
193 cells are key players²⁸. To model this process and analyse changes in miRNA gene expression, we
194 collected scRNA-seq profiles from conditions representing progressive atherosclerosis development in
195 LDLR^{-/-}ApoB^{100/100} mice fed with a chow or high fat diet (n=5 per group). The experimental setup led to
196 atherosclerotic plaque formation phenotype resembling early disease state (ED, shorter fat diet) and
197 late disease (LD, longer fat diet resulting in advanced vascular lesions) (Fig. 3A), confirmed by
198 examining the vessel wall cell phenotypes at lesions²⁹. In addition, we included lipopolysaccharide

199 (LPS) as an extra inflammatory stimulus introduced during the fat diet (two weeks prior to tissue
200 collection in ED condition) to achieve an inflammatory challenged state (IC, n=5) (Fig. 3A). In response
201 to IC and also at LD, the proportions of immune cells (T cells, B cells, and myeloid cells shown in Fig.
202 3B) were modulated, with concomitant decrease in relative proportion of non-immune tissue-resident
203 stromal cells. Among the immune cell types, the myeloid cell fraction increased the most between
204 different conditions.

205 To characterize further the myeloid compartment, we defined reproducible cell phenotype states by
206 computing a cell similarity graph from the scRNA-seq profiles using the MetaCell pipeline ³⁰. To
207 annotate the 27 nodes found that each represent a unique transcriptome state (Fig. 3C), we obtained
208 marker genes and visualized their expression alongside the expression of literature-based markers (Fig.
209 3D, Fig. S3A, Table S3A).

210 Macrophage (MP) markers were highly expressed in Nodes 1-10. Specifically, node 1 had elevated
211 expression of genes such as *Retnla* and *Fn1* (termed the reparatory-like MPs). Node 2 showed elevated
212 expression of *Trem2* that is a well-known marker of lipid-associated macrophages (termed the LAMs) ³¹.
213 Nodes 3 and 5-10 showed a higher expression of genes encoding for innate immune protein *C1q*
214 expression that in macrophages was previously suggested to alleviate inflammation present during
215 atherosclerosis disease progression ³². Accordingly, cells matched to nodes 5-10 predominantly
216 represented LD condition and showed a relatively higher expression of late-stage MP markers (*ApoE*,
217 *Selenop*, and *Cd63* ³³). In addition to node 2, nodes 5 and 6 had elevated expression of *Trem2*,
218 indicating a LAM-like transcriptional signature. Node 9 showed a high expression of *Cd163*, *Lyve1*, and
219 *Folr2* (termed as the tissue-resident MPs ³³). Interestingly, nodes 4 and 7 were enriched in genes
220 associated with chemokine-signaling such as *Cxcl2* and *Ccl4*, suggesting that node 4 is composed of
221 chemokine MPs and node 7 compose of *C1q+* MPs with also chemokine secretion. Additionally, node
222 7 showed an intermediate expression of *Cd163* and *Folr2* further implying a tissue-resident-like MP
223 phenotype.

224 Node 11 showed a distinct transcriptional state with a high expression of *Ccr7*, *Ccl22*, and *Fscn1* (Fig.
225 3D, Fig. S3A). Cell populations enriched with these markers have previously been termed the migratory
226 dendritic cells (DC) ³³ and the classical DC2A ³⁴. *Xcr1* and *Clec9a* were high expressed only in nodes
227 12 and 13 suggesting cDC1 phenotype ^{33,35}. Additionally, node 12 was enriched in genes encoding the
228 members of Cdc45/Mcm2-7/GINS (CMG) complex (*Mcm5* and *Mcm6*); thus, this node was termed as
229 proliferating cDC1. Nodes 14, 15, and 16 had elevated expression of *Cd209a* together with major
230 histocompatibility complex (MHC) II class genes (*H2-Eb1*, *H2-Ab1*, *H2-Aa*, *H2-DMb1*) and therefore
231 defined as MHCII DC ³³. Plasmacytoid DC markers (*Siglech*, *Ccr9*, *Cox6a2*, *Atp1b1*, *Ly6d* ³³) were
232 exclusively expressed in node 17.

233 Node 18 showed a mixture of different signatures: monocyte-derived MP (*Ccr2*), interferon (INF)
234 (*Isg15*), chemokine (*Cxcl10*), and active DNA replication (*Top2a*) suggesting that they are actively
235 replicating MPs undergoing transition potentially towards INF or chemokine MPs (Fig. 3D). Markers of
236 mixed Mo/MP (*Ccr2* together with *Fcgr1*, and *Itgam* ³³) were present in node 19. Since nodes 20-22

237 showed upregulation of *Ace* and *Ear2* together with downregulation of *Ccr2* and *Ly6c2*, they were
238 defined as non-classical monocytes (ncMo³³) (Fig. S3A). In contrast, nodes 24 and 27 showed
239 upregulation of *Ccr2* and *Ly6c2* together with high expression of *Chil3* and *Plac8*, and these nodes were
240 thus defined as classical monocytes (cMo³³). Nodes 23 and 25 showed mixed patterns of Mo and MP
241 such as intermediate expression of *Ccr2* (Mo-derived MP), *Isg15*, *Isg20* (INF), *Fcgr1*, and *Itgam* (Early
242 MP) (Fig. 3D). Node 26 was enriched in genes associated with INF signatures such as *Isg15* and *Isg20*
243 and was therefore defined as Mixed Mo (Fig. S3A).

244

245 Comparison of relative cell proportions revealed that macrophage nodes 1-3, 5-10, 19, and 23 had high
246 representation of cells in LD condition whereas ncMo nodes 20-22 and cMo/Mo-MP nodes 24-27 were
247 predominant in the IC condition (Fig. 3E, Fig. S3B). We next examined miRNA gene expression specific
248 to the metacell subpopulations. Highly node-specific expression of several immunomodulatory miRNA
249 genes distinguished the macrophage subtypes, in comparison to more subtle subtype-level differences
250 between DC and monocyte (Mo) cell subtypes (Fig. 3E). The macrophage miRNA markers included
251 highest mmu-mir-22 levels (regulation of proinflammatory cytokine expression³⁶) within reparatory MP,
252 LAM-specific expression of mmu-mir-23b~24-1~27b (regulation of proinflammatory cytokine
253 expression, downregulated miRNA in patients with autoimmune diseases³⁷), high mmu-mir-221~222
254 in *Cq1+* MP and mmu-mir-15a~16-1 (regulating phagocytosis³⁸) in MP node 7. The most distinct
255 miRNA gene expression among DC was found in cDC2 (e.g. mmu-mir-706 with possible unconventional
256 nuclear function³⁹) and in n15 cells corresponding to MHCII DC phenotype, that express mmu-mir-155,
257 known to function as a “master regulator miRNA” in DCs and MPs⁴⁰. In DCs mmu-mir-142a has key
258 role in regulation of proinflammatory cytokines in DCs⁴¹. In agreement, our analysis identified it as a
259 broadly expressed DC marker miRNA.

260 **Disease progression alters miRNA gene expression in macrophage subpopulations**

261 Next, we compared the miRNA gene expression distributions in ED and LD conditions in myeloid cells.
262 Across all cells, our analysis identified 21 upregulated and 6 downregulated miRNA genes (Fig. 4A, Fig.
263 S4A, Table S4). Among immunomodulatory miRNAs with potential to aggravate tissue inflammation,
264 we noted increased expression of mmu-mir-511⁴² driven by nodes 2-8 (Fig. 4A). An opposite change
265 was observed for mmu-mir-101b expression (negative regulator of pro-inflammatory response⁴³, with
266 strongest repression in nodes 23 and 25 (nodes panel, Fig. 4A). In comparison, immunosuppressive
267 mmu-mir-23b~24-1~27b expression increased in Trem2 and Trem2-like MPs (nodes 2 and 5) (nodes
268 panel, Fig. 4A) and miRNA genes encoding classical nuclear factor kappa B (NF-κB)-modulating
269 miRNAs mmu-mir-146a and mmu-mir-21⁴² increased in expression in several MP nodes, mmu-mir-
270 146a most strongly in node 7. Taken together, our results demonstrate that disease development
271 strongly modulates miRNA gene expression and that these changes include both pro- and anti-
272 inflammatory regulatory pathways with distinct expression across macrophage subtypes.

273 **Tissue-infiltration of monocytes and transition into mature phenotypes strongly modulates** 274 **miRNA gene expression**

275 The prominent increase in myeloid cells in adipose tissue at late disease, or at early disease upon LPS-
276 stimulus, prompted us next to examine changes in gene regulation during myeloid maturation into
277 tissue-resident cells. We hypothesized that the cytokine environment within tissue could trigger changes
278 in gene regulation and thereby miRNA expression. Thus, we collected additional scRNA-seq profiles
279 from blood monocytes and integrated these with the myeloid cell profiles from WAT. The monocytes in
280 blood are typically short-lived, representing a reference naïve state for the comparison. The cells
281 obtained from blood and WAT clustered primarily based on their tissue-of-origin (Fig. 5A, UMAP),
282 however with similar sub-populations (ncMO; cMO; DC) from both tissues placed adjacent to each
283 other, as defined using marker genes (Fig. S5A, see also Fig. 3 and Fig. S3). We focused on the main
284 monocyte and DC subtypes and performed statistical comparison of their tissue vs blood expression
285 profiles (Fig. 5B, Table S5A-B, refer also to Fig. S5B for DC comparison). In total, our analysis detected
286 significant changes in 45 and 95 miRNA genes in ncMo and cMo, respectively. Among the top
287 upregulated miRNA genes, mmu-mir-1938 and mmu-mir-22 are highly upregulated in both monocyte
288 types, while the most significant changes in cMo (more pro-inflammatory monocyte type) include also
289 upregulation of mmu-mir-221~222, mmu-mir-511, and mmu-mir-155. The comparison of top miRNAs
290 and classical LPS-responsive genes (*Dusp1*, *I11b*, *Ccl5*) in blood and WAT (Fig. 5C) highlights
291 increased expression of these pro-inflammatory genes (dot size and darker red color tone) upon tissue
292 infiltration that is further elevated in IC condition, most prominently in ncMo.

293 To validate that the changes detected from scRNA-seq profiles represent regulation of the
294 transcriptional activity at pri-miRNA loci, we used GRO-seq datasets (see Methods) collected from two
295 different experimental setups: *ex vivo* LPS stimulation of bone-marrow derived CD14+ macrophages
296 (referred to as BMDM) and LPS stimulation of peritoneal MPs (referred to as PM, resembling tissue-
297 resident MP). Three intergenic miRNA gene loci highlighted in the scRNA-seq analysis (Fig. 5A and B)
298 are shown in Fig. 5D. The elevated GRO-seq signal levels within the gene regions confirm that
299 upregulation of mmu-mir-22 and mmu-mir-221~222 transcription occurs rapidly in both BMDM and PM
300 cultures and remains high 180 h after LPS stimulus (see Table S5C-D for differential expression
301 statistics and summary). In comparison, mmu-mir-155 is significantly upregulated with delay at 60 h in
302 BMDM, representing a more immature cell model. In peritoneal cells its gene regulatory dynamics are
303 more rapid (upregulation at 1 h) and comparable to the two other miRNA loci, overall in agreement with
304 their increased expression in the tissue microenvironment and following LPS-stimulation in the *in vivo*
305 scRNA-seq profiles.

306

307 DISCUSSION

308 MiRNAs are key modulators in maintaining tissue homeostasis by post-transcriptionally regulating gene
309 expression. Thus, an imbalance in their expression has been associated with disease progression and
310 aging-related cellular processes including senescence^{44,45}. Here, we aimed to characterize miRNA
311 gene transcription in single-cell datasets to study cell-type specific miRNA expression. We provided
312 primary transcript annotations for mouse and human genomes that can be added to scRNA-seq
313 quantification pipelines and demonstrated feasibility to capture miRNA gene expression from both
314 droplet- and plate-based platforms. Based on this approach, we quantified and analysed miRNA gene
315 expression during aging in splenic immune cells and delineated changes in myeloid cell populations
316 upon atherosclerosis disease progression in blood and adipose tissue. The identified changes in miRNA
317 gene expression at cellular resolution include well-established miRNAs that control inflammation,
318 senescence, and metabolic responses in immune cells, supported by previous functional studies and
319 analysis of nascent transcription in *ex vivo* cell culture models. We provide the miRNA gene profiles
320 across the aging and atherosclerosis time series as an openly available resource to facilitate further
321 characterization of miRNA gene expression changes related to tissue homeostasis.

322 In this study, we extended reference transcript annotation with miRNA gene coordinates and evaluated
323 how two commonly used scRNA-seq platforms serve in miRNA gene detection and cell subpopulation
324 identification. The larger number of cells profiled using the 10x Genomics allows a better estimation of
325 the heterogeneity of a cell population^{7,46}. In line with previous results, the TMS 10x Genomics profiles
326 captured a higher proportion of non-coding transcripts compared to Smart-seq2 data⁷. Plate-based
327 studies, on the other hand, often aim at higher sequencing depth per cell and have full gene body signal
328 coverage. This could benefit the characterization of differences in alternative transcripts within miRNA
329 gene loci. However, if strand specificity is lacking, this analysis has similar limitations as chromatin
330 immunoprecipitation (ChIP)-seq based analysis of transcriptional activity, described in¹⁰. In both
331 platforms, the detection of miRNA gene transcription suffers from limited number of intronic reads
332 captured. In future, as more nascent transcriptome single cell profiles become available, better capture
333 of miRNA gene expression levels could be achieved. Among existing data, scRNA-seq profiles
334 generated from nuclei already provide higher capture of intronic reads⁴⁷ that will improve miRNA gene
335 detection⁴⁸. As the signal within pri-miRNA gene loci in standard scRNA-seq libraries can arise from
336 random priming at unspliced introns or polyA-based capture of incompletely processed primary
337 transcripts, we chose to base the miRNA gene annotation on integrated GRO-, CAGE- and ChIP-seq⁹
338 and Drosha knockout (KO) profiles⁴⁹, extending here to cover both human and mouse genomes.
339 Alternative transcript assembly-based approach⁵⁰ can leverage the data only partially, and as key
340 limitation its feasibility is impacted by insufficient cell numbers per cell type. Furthermore, quantification
341 of miRNA genes based on the pre-defined coordinates we provide here extends to other data types, as
342 it can be readily introduced into single-cell sequencing assay for transposase-accessible chromatin
343 (scATAC-seq) and scMultiome data analysis pipelines to analyse chromatin accessibility at miRNA loci,
344 enabling the identification of their corresponding regulatory elements residing in open chromatin.
345 Previous studies extending to chromatin signatures have provided key new insight on cell type-specific

346 gene regulatory network activity focusing on transcription factors⁵¹. The joint analysis of miRNA genes
347 will enable a more comprehensive analysis of gene regulatory networks that govern tissue homeostasis
348 at transcriptional and post-transcriptional levels.

349 Aging is a stepwise process characterized by changes in tissue homeostasis and cellular heterogeneity.
350 For example, changes in adipose depots distribution along the body dramatically affect tissue growth,
351 plasticity and function leading to metabolic dysfunction and low-grade inflammation⁵². Cross-talk
352 between adipose tissue and immune cells is crucial for the maintenance of normal healthy adipose
353 tissue function and systemic metabolism⁵³. Consequently, better understanding of the miRNA post-
354 transcriptional regulatory networks that fine tune cytokine expression and response dynamics upon
355 inflammatory challenge can provide new approaches to predict and prevent progression of age-related
356 functional changes⁵⁴. Mature miRNAs are highly stable and therefore ideal biomarker candidates for
357 monitoring disease progression. Moreover, new therapeutic approaches based on miRNA-delivery into
358 tissues are in development, with promise to reduce the burden of aging and immune dysfunction-related
359 disease including type 2 diabetes, atherosclerosis, dyslipidaemia, thermal dysregulation and skin ulcers
360 among others⁵⁵. In this study, we performed comparisons of miRNA gene expression in immune cells
361 from different tissues, including bone marrow-derived blood cells and more mature splenic and tissue-
362 resident populations. Our analysis identified altered expression of several miRNA genes (mmu-mir-101,
363 mmu-mir-30, mmu-mir-709) in spleen that have established function in regulation of
364 immunosenescence and apoptosis that throughout the body presents with alterations of immune cell
365 homeostasis and an overall decline in immune efficacy⁵⁶. The TMS atlas affords opportunity to extend
366 these comparisons to additional tissues. We limited the statistical comparisons to male mice, which is
367 different from earlier comparisons that included both sexes¹³. Our more conservative choice relates to
368 the lack of representation of both sexes in certain age groups, with more timepoints available in male
369 mice with sufficient time difference¹³. For example, in spleen tissue our analysis of male data included
370 young (1 and 3 months) versus old (21 and 30 months) comparison, while the female data corresponded
371 to adult (18 and 21 months) versus young (3 months) comparison. Concordantly, the profiles from our
372 atherosclerotic mouse model represent male mice, enabling comparison to TMS data without
373 confounding sex effect. The different aging profile of mmu-mir-146a in females suggests that miRNA
374 gene regulation is impacted by sex and is in agreement with a recent human study reporting that the
375 miR-146a age-related trajectory was confirmed only in men⁵⁷. Therefore, in future studies it would be
376 important to collect data representing more comprehensively both male and female aging. More
377 broadly, sex-biases in immune responses are well-established and known to strongly influence disease
378 prevalence^{58,59}. As the technologies mature, integrating cell-specific mature miRNA profiles will expand
379 the analysis of miRNA genes from the TMS and similar aging atlases, leading to better understand the
380 functional impact of miRNA dysregulation that can account for concomitant changes in RNA processing
381 that occur during aging^{60,61}, including decreased levels of the miRNA processing enzyme Dicer both in
382 mouse and human⁶². Furthermore, analysis of immune cell types at finer resolution should be pursued,
383 as was carried out here for myeloid cell subtypes, guided by updates to atlas cell type annotations and
384 improved understanding of the functional differences between the new cell subtypes identified from
385 single cell studies.

386 Traditionally, macrophages were categorized as pro-inflammatory (M1) and anti-inflammatory (M2)
387 macrophages that show distinct miRNA profiles, for example miR-511 expression is increased in M2
388 and decreased in M1 macrophages both *in vitro* and *in vivo* ⁶³. However, several studies have
389 suggested this dichotomy to be obsolete and that M1 and M2 stages rather represent the extremes of
390 a spectrum in a multidimensional space ^{64,65}. Recent single cell studies have characterized macrophage
391 subpopulations within the fat tissue, revealing subtypes involved in obesity disease progression,
392 including the description of Trem2+ lipid-associated macrophages ³⁴. Similarly, single cell profiling of
393 alveolar macrophages revealed novel macrophage subdivisions based on proliferation capacity and
394 inflammatory programming in the context of lung inflammation ⁶⁶. Here, we conducted analysis guided
395 by unbiased clustering of cells into nodes showing distinct transcriptional phenotypes. WAT myeloid
396 subtypes differed in miRNA gene expression, with highest basal miR-511 levels in tissue-resident
397 macrophages (nodes 9 and 10) and increased expression found across multiple subtypes upon disease
398 progression. The highest expressed miRNA genes in Trem2+ macrophages were mmu-mir-221~222
399 and mmu-mir-23b~24-1~27b loci. Previous studies have demonstrated a functional role for miR-
400 221/222 in inhibiting adipogenesis and preventing diet-induced obesity. At systemic level,
401 *Mir221/222AdipoKO* mice used in these studies did not show significant improvement of insulin
402 sensitivity. Instead, lower expression of these genes may promote apoptosis upon hyperglycaemia ⁶⁷.
403 Furthermore, mmu-mir-23b~24-1~27b locus from which miR-23b, miR-27b, miR-24-1 originate from
404 encodes miRNAs that each have a central role in regulation of lipid metabolism ⁶⁸⁻⁷⁰. Thus, changes in
405 their expression could strongly impact the lipid-associated functions of the Trem2+ cell phenotype.
406 Moreover, a recent study that generated a specific mouse KO of this miRNA locus showed impaired
407 glucose tolerance ⁷¹, emphasizing the critical role of miRNAs in maintenance of homeostasis. Here we
408 observed that upon inflammatory challenge (LPS stimulation) mmu-mir-221~222 expression increased,
409 while mmu-mir-23b~24-1~27b and *Trem2* levels decreased in the Trem2+ macrophage. Thus, future
410 studies examining the connection between Trem2-specific cell-intrinsic regulatory networks and
411 systemic glucose and lipid metabolism balance are warranted.

412 Infiltration of immune cells, especially those with pro-inflammatory function, into tissues is a known
413 hallmark of aging ⁵². We found that several key miRNA genes were regulated upon monocyte
414 recruitment into tissues. Among them, miR-155 induces pro-inflammatory activation of monocytes and
415 through increased expression of human leukocyte antigen (HLA)-DR in the myeloid cells, it also
416 modulates activation of T cells and can thereby aggravate tissue inflammation, promoting disease
417 progression in inflammatory-disease such as arthritis ⁷². However, the induction of mmu-mir-155
418 coincided with elevated expression of miRNA genes typical of M2-like cells, such as miR-146a and
419 miR-511 ⁷³. In addition, our analysis identified several less well-characterized miRNAs, including mmu-
420 mir-1938, that merit future functional characterization. The top target prediction for miR-1839 is *Laptm5*
421 (TargetScanMouse 7.1), encoding a lysosomal protein that modulates pro-inflammatory signalling in
422 macrophages ⁷⁴. Elucidating the mRNA targets using immunoprecipitation of argonaute family members
423 followed by RNA sequencing or reporter-based screens ⁷⁵ can provide a more comprehensive
424 understanding of how the miRNAs that are transcriptionally regulated upon tissue entry collectively
425 impact tissue cytokine environment, immune-cell interactions, and tissue homeostasis.

426 In summary, our work provides an unbiased and genome-wide evaluation of miRNA loci at cellular
427 resolution during aging and upon disease development and new tools for single-cell genomics research
428 to define miRNA regulatory networks with coordinated and cell type-specific activities across tissues.

429

430 **MATERIAL AND METHODS**

431 **Annotation of miRNA gene coordinates in mouse genome**

432 To distinguish primary transcripts corresponding to miRNA genes in mice, we followed the strategy we
433 introduced in ⁹. To define mouse pri-miRNA genes, GRO-seq and CAGE-seq data aligned to the mm9
434 genome were used to define genomic intervals that correspond to active primary transcription,
435 separated by active TSS. Due to fewer mouse GRO-seq samples available, the known RefSeq and
436 UCSC known gene (2018) transcript data ^{76,77} was included as external data to complement the *de*
437 *novo* transcript discovery. TSS coordinates were refined based on CAGE-seq, while the extension of
438 transcript ends was defined based on signal change point analysis from GRO-seq, or if the available
439 annotated gene region matched the candidate transcript the longer transcript region between the
440 annotated and discovered transcribed region was kept. Finally, the pre-miRNA annotations from
441 GenCode v19 and miRbase v.20 ⁶⁰ were used to annotate the subset of primary transcripts that
442 overlapped miRNA coordinates. The coordinates were then converted to mm10 using UCSC liftOver
443 tool ⁷⁸ to be compatible with the most recent genome version.

444

445 **Building a custom transcript annotation for scRNA-seq gene quantification workflows in mm10 446 and hg19 genomes**

447 Typical scRNA-seq quantification workflows, including the 10x Genomics Cell Ranger pipeline ⁷⁹, allow
448 users to build their own custom transcript annotation based on existing reference annotation data that
449 describes gene, transcript and exon information. To develop a custom reference suitable to quantify the
450 transcriptional activity of miRNA genes, we defined miRNA genes as the merged region starting from
451 the most distal TSS mapped to the miRNA and extending until the longest transcript end, using the
452 GRO- and CAGE-seq-based annotation for previously defined human coordinates⁹ and mouse
453 coordinates described above. This region was included in the GTF file as a single exon (pri-miRNA)
454 transcript. However, also alternative transcript and exon structures have been experimentally defined
455 for miRNA genes based on knockout of the key processing enzyme Drosha ⁴⁹. Therefore, the annotation
456 was extended by adding these candidate alternative transcript structures and at annotated coding gene
457 regions exons were included from GenCode (2018 and 2013 for mouse and human genomes
458 respectively), motivated by manual examination of splicing patterns captured in 10x Genomics and
459 Smart-seq2 scRNA-seq data. Cell Ranger requires that GTF files are preformatted using 'cellranger
460 mkgtf' command and that a FASTA file (reference genome) containing the nucleotide sequences of the
461 selected transcripts is provided. The generated GTF with miRNA genes and the FASTA file for mouse
462 mm10 or human hg19 genome were used as input for the 'cellranger mkref' command. The additional
463 quantification for the miRNA genes was combined in downstream analyses with the default GenCode-
464 based count matrix.

465

466 **TMS and Tabula Sapiens Data**

467 The TMS and Tabula Sapiens consortia generated single-cell libraries that were produced either using
468 single-cell suspensions combined with droplet detection (10x Genomics) or by fluorescence-activated
469 cell sorting (FACS) sorting individual cells combined with Smart-seq2 technology hereafter referred as
470 “Plate-seq” as denoted in the original TMS publications^{11–13,15}. In this work, we used data from spleen.
471 However quantified data is shared for Liver, Heart and Aorta, Fat and Bone Marrow tissues at 1 month,
472 3 months, 18 months, 21 months, 24 months, and 30 months of age for the tissues that were available.
473 Selected files were downloaded from the amazon cloud as described in the GitHub repository available
474 for this work (<https://github.com/anahSG/scMIR/>). A list of samples used can be found in Table S1D-E.

475

476 10x Genomics datasets were downloaded in .fastq format and processed with the default Cell Ranger
477 pipeline (v.3.0.2). The detection of cell-containing droplets in 10x Genomics data was performed using
478 the default count matrix, and the miRNA gene counts were added based on matching cell barcodes and
479 quantified with the option `–include-introns` (v.6.1.1). Smart-seq2 samples denoted as ‘Plate-seq’ were
480 downloaded in bam format and quantified with FeatureCounts (Subread package v.2.0.1,⁸⁰) using the
481 custom GTF reference genome with default options (in this case, the libraries are strandless).

482

483 Droplets assigned by the Cell Ranger pipeline as cell-containing droplets (filtered matrix) were further
484 quality controlled, filtered by QC metrics and processed using a standard SCANPY-based workflow
485 described in¹⁷ with minor modifications.

486

487 **Animal samples**

488 LDLR^{-/-}ApoB^{100/100} transgenic mice have a phenotype characterized by high accumulation of fat in the
489 tissues as they lack the ability to remove circulating lipid particles using the low-density lipoprotein
490 receptor (LDLR)^{81,82}. This model is commonly used to follow atherosclerotic plaque formation in veins
491 and arteries. To model disease progression, the transgenic mice were fed with a combination of chow
492 diet and after, fat diet (HFD; 0.2% total cholesterol, Teklad TD.88137) for one month, capturing early-
493 disease (ED) state. To study the impact of elevated pro-inflammatory signalling on immune cell tissue
494 infiltration during disease progression, mice following ED diet were injected with LPS during the HFD
495 phase two weeks prior to sacrifice. Late-disease (LD) state was achieved by feeding a fat diet for three
496 months²⁹. C57BL/6J mice fed with a chow diet were as an additional control for this study (see
497 annotation of cell types). We timed diet-starting age to equalize the age at sample collection between
498 all groups (8 months old). Throughout the study, mice were maintained on a 12-h light-dark cycle and
499 had access to food and water ad libitum.

500 All animal experiments were approved by the national Project Authorization Board (permission number
501 ESAVI/4567/2018) and were carried out in compliance with the EU Directive 2010/EU/63 on the
502 protection of animals used for scientific purposes.

503

504 **Tissue harvest, cell dissociation, and TotalSeq antibody staining**

505 Mice were anesthetized with isoflurane and euthanized by cervical dislocation. Cardiac puncture was
506 carried out with 10 mL of ice-cold PBS supplemented with 20 U/mL heparin and the mice were placed
507 into ice for dissection. ~200 mg of epididymal WAT of each mouse (n=3 for each condition) was minced
508 and added to 2.5 µl of Miltenyi Adipose Tissue Dissociation solution (supplemented with BSA and
509 HEPES) and incubated for 45 min at 37 °C on an end-over-end rotator. During dissociation, the tissue
510 was triturated 3 times (at 25 min, 35 min and 45 min) to break up cell aggregates. Tissue samples were
511 passed through a 30 µm cell strainer and washed with 3 ml of RPMI. Cells were centrifuged at 400 g
512 for 8 min at 4°C and the pellet was resuspended in 300 µl of FACS buffer (PBS with 1% BSA). Red
513 blood cells were lysed using 1X RBC Lysis Buffer, Multi-species (eBioscience #00-4300-54) by mixing
514 300 µl of cell suspension with 2.7 ml of ice cold 1X RBC lysis buffer and incubating for 3 min on ice. 2
515 ml of FACS buffer was added to normalize the buffer and the cells were collected by centrifugation at
516 400 g for 8 min at 4°C. After RBC lysis, the cells collected from each mouse were stained with Total-
517 Seq Mouse Hashtag antibody-DNA conjugates (BioLegend) containing a unique barcode sequence
518 according to the manufacturers' recommendations. The cell pellets were resuspended with TotalSeq
519 Mouse Hashtag Ab-DNA conjugate in FACS buffer. The cell suspension was incubated in ice for 15-20
520 min to allow for hashtag Ab binding. Afterwards, cells were washed two times with FACS buffer to
521 removed unbound hashtag Abs. Dead cells were removed with Miltenyi Dead Cell Removal kit (Miltenyi
522 Biotec #130-090-101) as described before (Örd et al., 2023). The cell pellets were resuspended in PBS
523 containing 0.04% BSA and counted by hemocytometry with trypan blue staining. Cell viability was
524 between 74% and 85%. For each condition, approximately 18,000 cells (pooled from 3 mice) were
525 loaded into the Chromium Controller microfluidics chip (10x Genomics).

526 Blood samples for monocyte isolation were processed by first performing erythrocyte lysis by mixing
527 aliquots of 500 µl of EDTA blood with 4.5 ml of ice-cold 1x RBC lysis buffer and incubating on ice for 3
528 min. Subsequently, cells were centrifuged at 500 g for 5 min at 4°C, supernatants were discarded, and
529 erythrocyte lysis was repeated. The cells were washed with 5 ml FACS buffer, followed by staining with
530 TotalSeq Mouse Hashtag Ab-DNA conjugates in FACS buffer for 15-20 min on ice. Following staining,
531 the cells were washed once with FACS buffer and once with MACS buffer (PBS with 0.5% BSA and
532 2mM EDTA). After staining, the CD115+ monocytes were enriched using Miltenyi Biotec MicroBead
533 kit (# 130-096-354) as described by the manufacturer. The stained cells from individual mice (three per
534 condition) were pooled in 90 µl MACS buffer, combined with 10 µl of the FcR Blocking Reagent (Miltenyi
535 Biotec), and incubated for 10 min at 4°C. 10 µl of CD115-Biotin conjugates were added and the
536 suspensions were mixed and incubated for 10 min at 4°C and the cells were pelleted by centrifugation
537 at 300 g for 5-10 min at 4°C. The supernatants were discarded, and the cell pellets were resuspended
538 in 80 µl of MACS buffer. 20 µl of Anti-Biotin MicroBeads were added to the solution, mixed and
539 incubated for 15 min at 4 °C. The cells were washed with 1-2 ml of MACS buffer and centrifuged at 300
540 g for 5-10 min at 4°C. The cells were resuspended in 500 µl of buffer. MS columns were placed in the
541 magnet and the samples were passed through 30 µm cell strainers before applying them to the MS
542 columns. All the subsequent steps were performed at 4°C. The columns were washed three times with

543 500 μ l of MACS buffer. After removing the column from the magnet, 1 ml of elution buffer was added,
544 and the cells were flushed out by firmly pushing the plunger into the column.

545 The cells collected from both tissues were centrifuged at 300 g for 5-10 min at 4 °C, resuspended in
546 PBS containing 0.04% BSA, and counted by hemocytometry with trypan blue staining. Cell viability was
547 between 74% and 85%. For each condition, approximately 30,000 cells (pooled from 3 mice) were
548 loaded into the Chromium Controller microfluidics chip (10x Genomics).

549 **Library preparation, sequencing, and alignment**

550 ScRNA-seq libraries were generated with the Chromium Single Cell 3' v.2 assay (10x Genomics).
551 Libraries were sequenced using the NovaSeq 6000 platform (Illumina) to a depth of approximately 300
552 million reads per library with read lengths of 26 (read 1) + 8 (i7 index) + 0 (i5 index) + 91 (read 2). Raw
553 reads were aligned to the mouse genome (mm10) using Cell Ranger (count pipeline) (v.3.0.2).

554

555 **scRNA-seq data integration and label transfer in the atherosclerotic mouse model**

556 Expression data was loaded in the Seurat R package v.4.0.0 for integration prior to cell type prediction.
557 Data was normalized using SCTransform to account for differences in sequencing depth. The reference
558 dataset used in integration was formed by the unbiased integration of the control (C57BL/6J on chow
559 diet) and late disease conditions for each tissue. The rest of the conditions were then integrated using
560 the canonical correlation (CCA) algorithm (k.anchor=20, dims = 1:50). Cell type predictions at broad
561 lineage level were obtained by performing tissue-wide label transfer. WAT labels were transferred from
562 the TMS fat dataset. Blood tissue labels were transferred from the 10x Genomics Peripheral blood
563 mononuclear cell (PBMC) human reference dataset ⁷⁹. Gene symbols were translated to mouse with
564 the biomaRt R package v.2.54.1 ^{83,84}.

565

566 **Data de-multiplexing by hashtag signals**

567 The atherosclerotic mouse model samples were hashtag-barcoded with individual barcodes added to
568 distinguish between mice. Tissues including WAT and aorta yielded initially very low signal in cells
569 detected by Cell Ranger, resulting in ~80% negative cells with default demultiplexing settings (mostly
570 in cells that were annotated as stromal cells). To overcome this limitation, we used the DSB R library
571 v.1.0.3 ⁸⁵ that was built to estimate the difference between the actual antibody signal in cell-containing
572 droplets and the background signal in empty droplets in cellular indexing of transcriptomes and epitopes
573 (CITE)-seq single-cell libraries. The DSB workflow uses the raw matrices containing all the droplets
574 available and produces a matrix of scaled protein signals vs the background signal. We used the
575 hashtag scaled matrix as input to perform the hashtag based demultiplexing. We also noticed that the
576 differences in the distribution of hashtag signal intensity between cells of distinct lineage (e.g. myeloid
577 vs. lymphoid) were causing errors in the annotation of doublets across the tissue (proportions of
578 negative cells or doublets would not typically be expected to vary by cell type). To overcome this, we
579 performed the hashtag demultiplexing separately by the broad cell lineage annotation obtained using
580 label transfer. We continued the analysis with cells that were annotated as individual cells (singlets) and
581 repeated the sample integration.

582

583 **scRNA-seq quality filtering and normalization**

584 To check the quality of the libraries generated, we followed a basic QC and filtering workflow using the
585 SCANPY v.1.8.2 package for each tissue. Transcripts were filtered to include those that were present
586 in more than 3 cells. To assess the viability of the cells, we quantified mitochondrial and ribosomal
587 genes. Cells were filtered out according to a maximum mitochondrial gene expression percentage, a
588 maximum number of counts and a minimum number of expressed genes. Due to heterogeneity in the
589 raw data, these parameters were set for each tissue and condition (refer to TableS3).

590

591 Expression data was normalized with size factor values derived from data normalization using the scanpy
592 R package v.1.26.2, and then log-transformed using the function `scanpy.pp.log1p`. Highly variable
593 genes were calculated with `scanpy.pp.highly_variable_genes`, selecting the top 4000 genes for principal
594 component analysis and dimensional reduction. Louvain and Leiden clustering at different resolutions
595 were performed to define similar transcriptome states that can be used for assigning lineage and cell
596 type annotations.

597

598 **Differential expression analysis using scDD**

599 The log₂ counts based on vst transformation available in Seurat R package v.4.0.1 were used to
600 compare differences in gene expression distributions in a given cell type between different sample
601 groups (e.g. young and old, or late vs. early disease) using the scDD v.1.14⁸⁶ package following the
602 approach described in⁸⁷. This statistical analysis allows the detection of expression changes based on
603 the fraction of cells expressing a certain transcript (DZ category) and among expressing cells by
604 comparing the expression level (DE, DP and DM categories)⁸⁶. Transcripts with adj. p-value < 0.05
605 (Benjamini-Hochberg FDR method) were considered as significant.

606

607 Combined p-values were calculated based on the Fisher's exact test (sumlog function from metap R
608 package v.1.8) across all cell types to identify miRNAs that were concordantly regulated during aging.
609 From those, miRNAs with associated p-values < 0.05 that passed a log fold change cut-off in at least
610 two cell types were considered as top-ranking candidates presented in figures.

611

612 **MetaCell analysis of tissue myeloid cell sub-populations**

613 Myeloid cells extracted from white adipose tissue samples were used to compute a cell similarity graph
614 to obtain homogenous group of cells denoted as 'metacells' with the MetaCell R package v.0.3.7³⁰.
615 Gene-level statistics were computed with 'mcell_add_gene_stat' and featured genes were selected
616 based on their variance (>0.8, 'mcell_gsetfilter_varmean') and number of UMIs (>100 UMIs in the entire
617 dataset and selected genes are required to be detected in at least 3 cells with > 2 UMIs,
618 'mcell_gset_filter_cov'). A balanced cell graph or 'balanced K-nn graph' was computed as previously
619 described (K=100, 'mcell_add_cgraph_from_mat_bknn'). Next, we performed resampling (n=500) and
620 generated the co-clustering graph ('mcell_coclust_from_graph_resamp', min. node size=20, cell
621 partitions= 5.000 covering 75% of the cells). Metanodes assignment-derived statistics from the co-

622 clustering step are evaluated with 'mcell_mc_from_coclust_balanced' command with default settings.
623 To check that the metacell nodes are homogeneous, cells that highly deviate from their metacell's
624 expression profile were plotted as outlier cells ('mcell_plot_outlier_heatmap', data not shown) and
625 filtered afterwards 'mcell_mc_split_filt'. Gene markers per node were extracted for further analysis –
626 'mcell_gset_from_mc_markers'. Metacells were projected into a 2D graph for visualization
627 ('mcell_mc2d_force_knn', 'mcell_mc2d_plot').

628

629 **Differential expression analysis of bulk GRO-seq profiles from macrophage *ex vivo* cultures**

630 Samples listed in Table S1A were used for differential expression testing as previously described in ⁹.
631 Low expressed transcripts were filtered and differences in transcription level between sample groups
632 analyzed with limma and edgeR packages. Genes were assigned significant based on adjusted p-value
633 < 0.05 (Benjamini-Hochberg method).

634

635 **AVAILABILITY**

636 Data analysis code and links to .h5ad files comprising quantified scRNA-seq data objects with miRNA
637 genes are available under GitHub repository (<https://github.com/anahSG/scMIR/>).

638 **ACCESSION NUMBERS**

639 NGS data has been submitted to NCBI GEO data repository with the accession codes GSE241552:
640 obebmimixdoztsv, (scRNA-seq from atherosclerosis mouse model), GSE241567: armhsaqyfxgzlmr
641 (scRNA-seq in ST2 cell line), GSE241550: ololkqcgrxkfrax (new GRO-seq data generated for primir
642 transcript detection). Other accession codes for datasets used in analysis are listed in Table S1A.

643 **SUPPLEMENTARY DATA**

644 **ACKNOWLEDGEMENT**

645 The authors wish to acknowledge UEF Bioinformatics Center (Biocenter Finland) and CSC – IT Center
646 for Science, Finland, for computational resources; Turku single-cell omics core facility services
647 (Biocenter Finland), Turku Bioscience and EMBL GeneCore sequencing team for sequencing service
648 provided; Turku Center for Disease Modeling University of Turku TCDM (European Infrastructure for
649 Translational Medicine) for animal housing. We would like to acknowledge researchers who shared
650 their data in NCBI-GEO or public repositories and made it available. We gratefully acknowledge group
651 members (Petri Pölönen, Juha Mehtonen and Minna Voutilainen) for assistance in miRNA gene
652 analysis and Juha Kekäläinen and Buddika Jayasingha for assistance in data sharing.

653 **FUNDING**

654 This work was supported by the Academy of Finland grants [3145553, 335964 to M.H; 335973,314554,
655 to M.U.K; 314556, 335975 to A.R and 335977, 314557 to T.L], Jane and Aatos Erkkö Foundation to
656 A.R., the Finnish Cultural Foundation to A.H.S., and Fondation du Pélican de Marie et Pierre Hippert-
657 Faber (Luxembourg) Graduate Fellowship to M.B.L.

658 AUTHOR CONTRIBUTIONS

659 **AH de Sande:** Conceptualization, Data curation, Analysis, Methodology, Visualization, Writing the
660 manuscript. **T Turunen:** Analysis, Visualization, Writing the manuscript. **M Bouvy-Liivrand:**
661 Conceptualization, Experimental design, Sample collection, Methodology, Analysis, Supervision. **T**
662 **Örd:** Design of the animal study, Animal work, Sample collection, NGS library preparation. **C Tundidor-**
663 **Centeno:** Data curation, Analysis, Visualization. **H Liljenbäck:** Animal work, Sample collection. **S**
664 **Palani:** Design of the animal study, Animal work, Sample collection. **J Virta:** Animal work, Sample
665 collection. **OP Smolander:** Supervision. **A Roivainen:** Design of animal study, funding acquisition,
666 Supervision. **T Lönnberg:** Design of the animal study, Sample collection, NGS library preparation,
667 Funding acquisition. **MU Kaikkonen:** Design of the animal study, Supervision, Funding acquisition. **M**
668 **Heinäniemi:** Conceptualization, Design of the animal study, Analysis, Methodology, Funding
669 acquisition, Project administration, Writing the manuscript.

670 CONFLICT OF INTEREST

671 The authors declare that they have no known competing financial interests or personal relationships
672 that could have appeared to influence the work reported in this paper.

673 FIGURE LEGENDS

674 **Figure 1. miRNA gene annotation and quantification in scRNA-seq datasets.** (A) Overview of the
675 miRNA gene quantification for scRNA-seq data. Gene and miRNA gene counts were extracted with the
676 Cell Ranger or FeatureCounts pipelines, followed by downstream analysis performed by combining
677 Seurat⁸⁸ and SCANPY⁸⁹ packages to obtain and study cell-type-specific miRNA gene expression at
678 single-cell resolution. (B) miRNA gene markers (n=6 per cell type, defined from mouse droplet-based
679 10x Genomics data in grey shade) were compared to their corresponding human genes and mature
680 forms in splenic cells including B-cell, NK-cell, and T-cell subpopulations. On the left, dot plot heatmaps
681 shows miRNA gene expression (from high expression in yellow to low expression in blue) and
682 percentage of expression (circle size) based on 10x Genomics and FACS-coupled Smart-seq2
683 technology in mouse. On the right, the heatmap depicts mature miRNA expression levels from FACS-
684 sorted splenic cells measured with PCR (GSE144081 from¹⁶). * mouse miRNA genes that were not
685 annotated in the human genome. (C) Comparison of scRNA-seq-based quantification (log₂ miRNA
686 gene expression) to GRO-seq-based primary transcript expression in the mouse stromal cell line ST2.
687 Genes were binned from low to high expression levels based on GRO-seq data (lower panel) or scRNA-
688 seq data (upper panel).

689 **Figure 2. Differential expression analysis of miRNA genes in spleen tissue during aging.** (A)
690 Uniform manifold approximation and projection (UMAP) plot of the integrated spleen (all age groups)
691 dataset (n=27260 cells). Colors indicating different cell types (annotations from TMS) from 8 major
692 clusters (n>150 cells) include B cells (n=18398) in dark blue, T cells (n=4029) in forest green, mature
693 NK T cells (n=2131) in light blue, macrophages (n=652) in olive green, NK cells (n=385) in orange,
694 proerythroblast (n=464) in coral red, plasma cells (n=559) in light green and dendritic cells (n=249) in
695 red). (B) Cell type percentages from male mice present in each age group of the dataset are shown as
696 a line plot. (C) The number of DZ and DE miRNAs detected in each cell type separated by up and
697 downregulated genes are shown (dark green and light green respectively). (D) Heatmap showing top
698 ranked miRNA genes that were differentially detected (DZ) across main cell types in the spleen (Fisher's
699 exact test associated p value < 0.05, absolute log₂ FC>0.5). Fold changes between old and young cells
700 are shown in each cell type. (E) Dot plot heatmaps of myeloid-specific changes in miRNA gene levels
701

702 (adjust p value <0.05). (F) UMAP plots of macrophage and dendritic cell gene markers (on the left) and
703 cell type-specific miRNAs (on the right).

704 **Figure 3. Characterization of myeloid cell subpopulations and their miRNA gene profiles during**
705 **atherosclerosis disease progression.** (A) Scheme of the study of atherosclerotic plaque formation in
706 mice. Mice were fed either a chow diet (in green) or fat diet (in gold). Samples were denoted as early-
707 disease (ED), inflammatory challenge (IC) and late-disease (LD) for LDL deficient mice. (B) Proportion
708 of cell types across the sample types. (C) Cells grouped in meta nodes based on their reproducible
709 phenotypes. (D) Heatmap showing expression of selected node marker genes (above) and marker
710 miRNA genes (below). Expression is row-scaled. (E) Changes in cell proportions between ED and LD
711 conditions (above) and between ED and IC conditions (below).

712 **Figure 4. Disease progression alters miRNA gene expression in macrophage subpopulations.**
713 miRNA genes with altered expression during disease progression are shown as dot plot heatmap and
714 stratified by metanode. Brighter color tone and larger dot size denote higher expression.

715 **Figure 5. Gene expression changes in monocytes infiltrating adipose tissue relative to naïve**
716 **blood precursors.** (A) UMAP of blood and tissue (WAT) myeloid cell populations. (B) Volcano plots
717 representing significant miRNA gene loci from tissue vs blood comparison of monocyte subtypes. Top
718 miRNA loci are indicated on the plot. FC correspond to differences in detection rate. (C) Dot plot
719 heatmap comparing known LPS-responsive genes to the profile of top miRNA loci in tissue and blood.
720 (D) GRO seq signal tracks at mmu-mir-22, mmu-mir-155 and mmu-mir-221~222 loci. The + strand
721 signal is shown above the vertical axis (dark red tone) and -strand signal below (light red tone). NcMo:
722 non-classical monocyte, cMo: classical monocyte, DC: dendritic cell, ED: early disease, IC:
723 inflammatory challenge, BMDM: bone-marrow derived macrophage, PM: peripheral macrophage, LPS:
724 lipopolysaccharide, KLA: Kdo2-lipid A).

725

726 REFERENCES

- 727 1. Paul, F. *et al.* Transcriptional Heterogeneity and Lineage Commitment in Myeloid Progenitors.
728 *Cell* **164**, 325 (2016).
- 729 2. Bartel, D. P. MicroRNAs: Genomics, Biogenesis, Mechanism, and Function. *Cell* **116**, 281–297
730 (2004).
- 731 3. Franceschi, C., Garagnani, P., Parini, P., Giuliani, C. & Santoro, A. Inflammaging: a new
732 immune–metabolic viewpoint for age-related diseases. *Nat. Rev. Endocrinol.* **14**, 576–590 (2018).
- 733 4. Leonardi, G. C., Accardi, G., Monastero, R., Nicoletti, F. & Libra, M. Ageing: from inflammation to
734 cancer. *Immun. Ageing* **15**, 1 (2018).
- 735 5. Benesova, S., Kubista, M. & Valihrach, L. Small RNA-Sequencing: Approaches and
736 Considerations for miRNA Analysis. *Diagnostics* **11**, 964 (2021).
- 737 6. Faridani, O. R. *et al.* Single-cell sequencing of the small-RNA transcriptome. *Nat. Biotechnol.* **34**,
738 1264–1266 (2016).

- 739 7. Wang, X., He, Y., Zhang, Q., Ren, X. & Zhang, Z. Direct Comparative Analyses of 10X Genomics
740 Chromium and Smart-seq2. *Genomics Proteomics Bioinformatics* **19**, 253–266 (2021).
- 741 8. La Manno, G. *et al.* RNA velocity of single cells. *Nature* **560**, 494–498 (2018).
- 742 9. Bouvy-Livrand, M. *et al.* Analysis of primary microRNA loci from nascent transcriptomes reveals
743 regulatory domains governed by chromatin architecture. *Nucleic Acids Res.* **45**, 9837–9849
744 (2017).
- 745 10. Turunen, T., Hernández De Sande, A., Pölönen, P. & Heinäniemi, M. Genome-wide analysis of
746 primary microRNA expression using H3K36me3 ChIP-seq data. *Comput. Struct. Biotechnol. J.*
747 **19**, 1944–1955 (2021).
- 748 11. Almanzar, N. *et al.* A single-cell transcriptomic atlas characterizes ageing tissues in the mouse.
749 *Nature* **583**, 590–595 (2020).
- 750 12. Schaum, N. *et al.* Single-cell transcriptomics of 20 mouse organs creates a Tabula Muris. *Nature*
751 **562**, 367–372 (2018).
- 752 13. Schaum, N. *et al.* Ageing hallmarks exhibit organ-specific temporal signatures. *Nature* **583**, 596–
753 602 (2020).
- 754 14. Picelli, S. *et al.* Full-length RNA-seq from single cells using Smart-seq2. *Nat. Protoc.* **9**, 171–181
755 (2014).
- 756 15. The Tabula Sapiens Consortium. The Tabula Sapiens: A multiple-organ, single-cell transcriptomic
757 atlas of humans. *Science* **376**, eabl4896 (2022).
- 758 16. Rose, S. A. *et al.* A microRNA expression and regulatory element activity atlas of the mouse
759 immune system. *Nat. Immunol.* **22**, 914–927 (2021).
- 760 17. The Tabula Muris Consortium *et al.* A single-cell transcriptomic atlas characterizes ageing tissues
761 in the mouse. *Nature* **583**, 590–595 (2020).
- 762 18. Smith-Vikos, T. & Slack, F. J. MicroRNAs and their roles in aging. *J. Cell Sci.* **125**, 7–17 (2012).
- 763 19. Nunes, A. D. C. *et al.* miR-146a-5p modulates cellular senescence and apoptosis in visceral
764 adipose tissue of long-lived Ames dwarf mice and in cultured pre-adipocytes. *GeroScience* **44**,
765 503–518 (2022).
- 766 20. Victoria, B. *et al.* Circulating microRNA signature of genotype-by-age interactions in the long-lived
767 Ames dwarf mouse. *Aging Cell* **14**, 1055–1066 (2015).

- 768 21. Lin, L. & Hu, K. MiR-147: functions and implications in inflammation and diseases. *Microna* **10**,
769 91–96 (2021).
- 770 22. Yin, R., Guo, D., Zhang, S. & Zhang, X. miR-706 inhibits the oxidative stress-induced activation of
771 PKC α /TAOK1 in liver fibrogenesis. *Sci. Rep.* **6**, 37509 (2016).
- 772 23. Martinez, I., Cazalla, D., Almstead, L. L., Steitz, J. A. & DiMaio, D. miR-29 and miR-30 regulate
773 B-Myb expression during cellular senescence. *Proc. Natl. Acad. Sci. USA* **108**, 522–527 (2011).
- 774 24. Liao, L. *et al.* Redundant miR-3077-5p and miR-705 mediate the shift of mesenchymal stem cell
775 lineage commitment to adipocyte in osteoporosis bone marrow. *Cell Death Dis.* **4**, e600 (2013).
- 776 25. Yao, J. *et al.* Possible role of microRNA miRNA-IL-25 interaction in mice with ulcerative colitis.
777 *Bioengineered* **11**, 862–871 (2020).
- 778 26. Ito, Y. *et al.* Both microRNA-455-5p and -3p repress hypoxia-inducible factor-2 α expression and
779 coordinately regulate cartilage homeostasis. *Nat. Commun.* **12**, 4148 (2021).
- 780 27. Rivetti di Val Cervo, P. *et al.* p63–microRNA feedback in keratinocyte senescence. *Proc. Natl.*
781 *Acad. Sci. U.S.A.* **109**, 1133–1138 (2012).
- 782 28. Mathis, D. Immunological Goings-on in Visceral Adipose Tissue. *Cell Metab.* **17**, 851–859 (2013).
- 783 29. Örd, T. *et al.* Dissecting the polygenic basis of atherosclerosis via disease-associated cell state
784 signatures. *Am. J. Hum. Genet.* **110**, 722–740 (2023).
- 785 30. Baran, Y. *et al.* MetaCell: analysis of single-cell RNA-seq data using K-nn graph partitions.
786 *Genome Biol.* **20**, 206 (2019).
- 787 31. Jaitin, D. A. *et al.* Lipid-Associated Macrophages Control Metabolic Homeostasis in a Trem2-
788 Dependent Manner. *Cell* **178**, 686-698.e14 (2019).
- 789 32. Spivia, W., Magno, P. S., Le, P. & Fraser, D. A. Complement protein C1q promotes macrophage
790 anti-inflammatory M2-like polarization during the clearance of atherogenic lipoproteins. *Inflamm.*
791 *Res.* **63**, 885–893 (2014).
- 792 33. Jung, S.-H. *et al.* Spatiotemporal dynamics of macrophage heterogeneity and a potential function
793 of Trem2hi macrophages in infarcted hearts. *Nat. Commun.* **13**, 1–15 (2022).
- 794 34. Hildreth, A. D. *et al.* Single-cell sequencing of human white adipose tissue identifies new cell
795 states in health and obesity. *Nat. Immunol.* **22**, 639–653 (2021).
- 796 35. Dick, S. A. *et al.* Self-renewing resident cardiac macrophages limit adverse remodeling following
797 myocardial infarction. *Nat. Immunol.* **20**, 29–39 (2019).

- 798 36. Youn, G. S. *et al.* MicroRNA-22 negatively regulates LPS-induced inflammatory responses by
799 targeting HDAC6 in macrophages. *BMB Rep.* **53**, 223–228 (2020).
- 800 37. Zhang, Y. *et al.* miR-23b Suppresses Leukocyte Migration and Pathogenesis of Experimental
801 Autoimmune Encephalomyelitis by Targeting CCL7. *Mol. Ther.* **26**, 582–592 (2018).
- 802 38. Moon, H.-G., Yang, J., Zheng, Y. & Jin, Y. miR-15a/16 Regulates Macrophage Phagocytosis
803 After Bacterial Infection. *J. Immunol.* **193**, 4558–4567 (2014).
- 804 39. Wong, J. J. *et al.* Identification of nuclear-enriched miRNAs during mouse granulopoiesis. *J.*
805 *Hematol. Oncol.* **7**, 42 (2014).
- 806 40. Dueck, A., Eichner, A., Sixt, M. & Meister, G. A miR-155-dependent microRNA hierarchy in
807 dendritic cell maturation and macrophage activation. *FEBS Lett.* **588**, 632–640 (2014).
- 808 41. Sun, Y. *et al.* Targeting of microRNA-142-3p in dendritic cells regulates endotoxin-induced
809 mortality. *Blood* **117**, 6172–6183 (2011).
- 810 42. Rahman, S. *et al.* miR-511 Deficiency Protects Mice from Experimental Colitis by Reducing TLR3
811 and TLR4 Responses via WD Repeat and FYVE-Domain-Containing Protein 1. *Cells* **11**, 58
812 (2022).
- 813 43. Liu, D. *et al.* Dysregulated expression of miR-101b and miR-26b lead to age-associated increase
814 in LPS-induced COX-2 expression in murine macrophage. *Age* **37**, 97 (2015).
- 815 44. Choi, S. W., Lee, J. Y. & Kang, K.-S. miRNAs in stem cell aging and age-related disease. *Mech.*
816 *Ageing Dev.* **168**, 20–29 (2017).
- 817 45. Eshkoor, S. A., Ghodsian, N. & Akhtari-Zavare, M. MicroRNAs influence and longevity. *Egypt. J.*
818 *Med. Hum. Genet.* **23**, 105 (2022).
- 819 46. Baran-Gale, J., Chandra, T. & Kirschner, K. Experimental design for single-cell RNA sequencing.
820 *Brief. Funct. Genom.* **17**, 233–239 (2018).
- 821 47. Bakken, T. E. *et al.* Single-nucleus and single-cell transcriptomes compared in matched cortical
822 cell types. *PLoS One* **13**, e0209648 (2018).
- 823 48. Elias, A. E., Nuñez, T. A., Kun, B. & Kreiling, J. A. primiReference: a reference for analysis of
824 primary-microRNA expression in single-nucleus sequencing data. *J. Genet. Genomics* **50**, 108–
825 121 (2023).

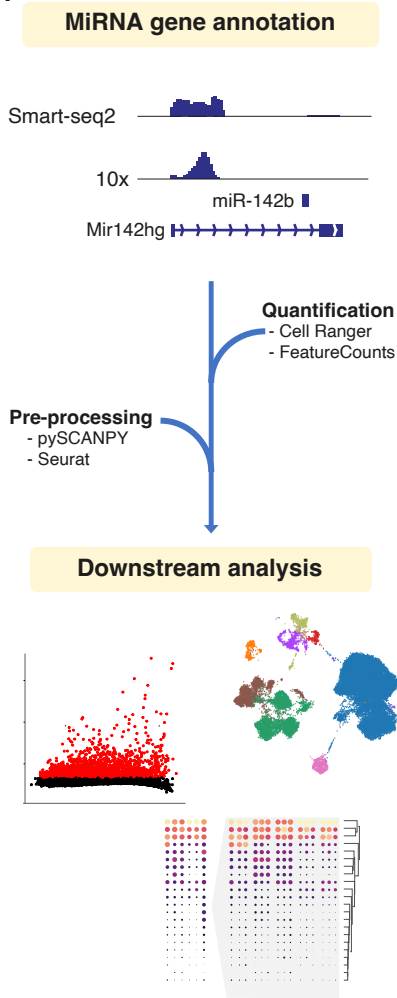
- 826 49. Chang, T.-C., Pertea, M., Lee, S., Salzberg, S. L. & Mendell, J. T. Genome-wide annotation of
827 microRNA primary transcript structures reveals novel regulatory mechanisms. *Genome Res.* **25**,
828 1401–1409 (2015).
- 829 50. Ji, J., Anwar, M., Petretto, E., Emanuelli, C. & Srivastava, P. K. PPMS: A framework to Profile
830 Primary MicroRNAs from Single-cell RNA-sequencing datasets. *Brief. Bioinformatics* **23**, bbac419
831 (2022).
- 832 51. Jansen, C. *et al.* Building gene regulatory networks from scATAC-seq and scRNA-seq using
833 Linked Self Organizing Maps. *PLoS Comput. Biol.* **15**, e1006555 (2019).
- 834 52. Zamboni, M., Nori, N., Brunelli, A. & Zoico, E. How does adipose tissue contribute to
835 inflammaging? *Exp. Gerontol.* **143**, 111162 (2021).
- 836 53. Chung, H. Y. *et al.* Redefining Chronic Inflammation in Aging and Age-Related Diseases:
837 Proposal of the Senoinflammation Concept. *Aging Dis.* **10**, 367–382 (2019).
- 838 54. Garg, D. & Cohen, S. M. miRNAs and aging: A genetic perspective. *Ageing Res. Rev.* **17**, 3–8
839 (2014).
- 840 55. Cartwright, M., Tchkonja, T. & Kirkland, J. Aging in adipocytes: Potential impact of inherent,
841 depot-specific mechanisms. *Exp. Gerontol.* **42**, 463–471 (2007).
- 842 56. Wang, Y., Dong, C., Han, Y., Gu, Z. & Sun, C. Immunosenescence, aging and successful aging.
843 *Front. Immunol.* **13**, (2022).
- 844 57. Mensà, E. *et al.* Circulating miR-146a in healthy aging and type 2 diabetes: Age- and gender-
845 specific trajectories. *Mech. Ageing Dev.* **180**, 1–10 (2019).
- 846 58. Klein, S. L. & Flanagan, K. L. Sex differences in immune responses. *Nat. Rev. Immunol.* **16**, 626–
847 638 (2016).
- 848 59. Olivieri, F. *et al.* Sex/gender-related differences in inflammaging. *Mech. Ageing Dev.* **211**, 111792
849 (2023).
- 850 60. Johnson, A. A. *et al.* The Role of DNA Methylation in Aging, Rejuvenation, and Age-Related
851 Disease. *Rejuvenation Res.* **15**, 483–494 (2012).
- 852 61. Harries, L. W. MicroRNAs as Mediators of the Ageing Process. *Genes* **5**, 656–670 (2014).
- 853 62. Mori, M. A. *et al.* Role of MicroRNA Processing in Adipose Tissue in Stress Defense and
854 Longevity. *Cell Metab.* **16**, 336–347 (2012).

- 855 63. Karo-Atar, D., Itan, M., Pasmanik-Chor, M. & Munitz, A. MicroRNA profiling reveals opposing
856 expression patterns for miR-511 in alternatively and classically activated macrophages. *J.*
857 *Asthma* **52**, 545–553 (2015).
- 858 64. Ginhoux, F., Schultze, J. L., Murray, P. J., Ochando, J. & Biswas, S. K. New insights into the
859 multidimensional concept of macrophage ontogeny, activation and function. *Nat. Immunol.* **17**,
860 34–40 (2016).
- 861 65. Xue, J. *et al.* Transcriptome-Based Network Analysis Reveals a Spectrum Model of Human
862 Macrophage Activation. *Immunity* **40**, 274–288 (2014).
- 863 66. Mould, K. J., Jackson, N. D., Henson, P. M., Seibold, M. & Janssen, W. J. Single cell RNA
864 sequencing identifies unique inflammatory airspace macrophage subsets. *JCI Insight* **4**, (2019).
- 865 67. Monteiro, M. M. *et al.* Lowered Expression of MicroRNAs 221 and 222 Mediate Apoptosis
866 Induced by High Glucose in Human Periodontal Ligament Cells. *Cell Biochem. Biophys.* **78**, 391–
867 398 (2020).
- 868 68. Vickers, K. C. *et al.* MicroRNA-27b is a regulatory hub in lipid metabolism and is altered in
869 dyslipidemia. *Hepatology* **57**, 533–542 (2013).
- 870 69. Li, L. *et al.* miR-23a/b-3p promotes hepatic lipid accumulation by regulating Srebp-1c and Fas. *J.*
871 *Mol. Endocrinol.* **68**, 35–49 (2022).
- 872 70. Ng, R. *et al.* Inhibition of microRNA-24 expression in liver prevents hepatic lipid accumulation and
873 hyperlipidemia. *Hepatology* **60**, 554–564 (2014).
- 874 71. Jiang, Y.-H. *et al.* Loss of miR-23b/27b/24-1 Cluster Impairs Glucose Tolerance via Glycolysis
875 Pathway in Mice. *Int. J. Mol. Sci.* **22**, 550 (2021).
- 876 72. Olsson, A. M. *et al.* miR-155-overexpressing monocytes resemble HLA^{high}ISG15⁺ synovial
877 tissue macrophages from patients with rheumatoid arthritis and induce polyfunctional CD4⁺ T-cell
878 activation. *Clin. Exp. Immunol.* **207**, 188–198 (2021).
- 879 73. Alwani, A., Andreasik, A., Szatanek, R., Siedlar, M. & Baj-Krzyworzeka, M. The Role of miRNA in
880 Regulating the Fate of Monocytes in Health and Cancer. *Biomolecules* **12**, 100 (2022).
- 881 74. Glowacka, W. K., Alberts, P., Ouchida, R., Wang, J.-Y. & Rotin, D. LAPTM5 Protein Is a Positive
882 Regulator of Proinflammatory Signaling Pathways in Macrophages. *J. Biol. Chem.* **287**, 27691–
883 27702 (2012).

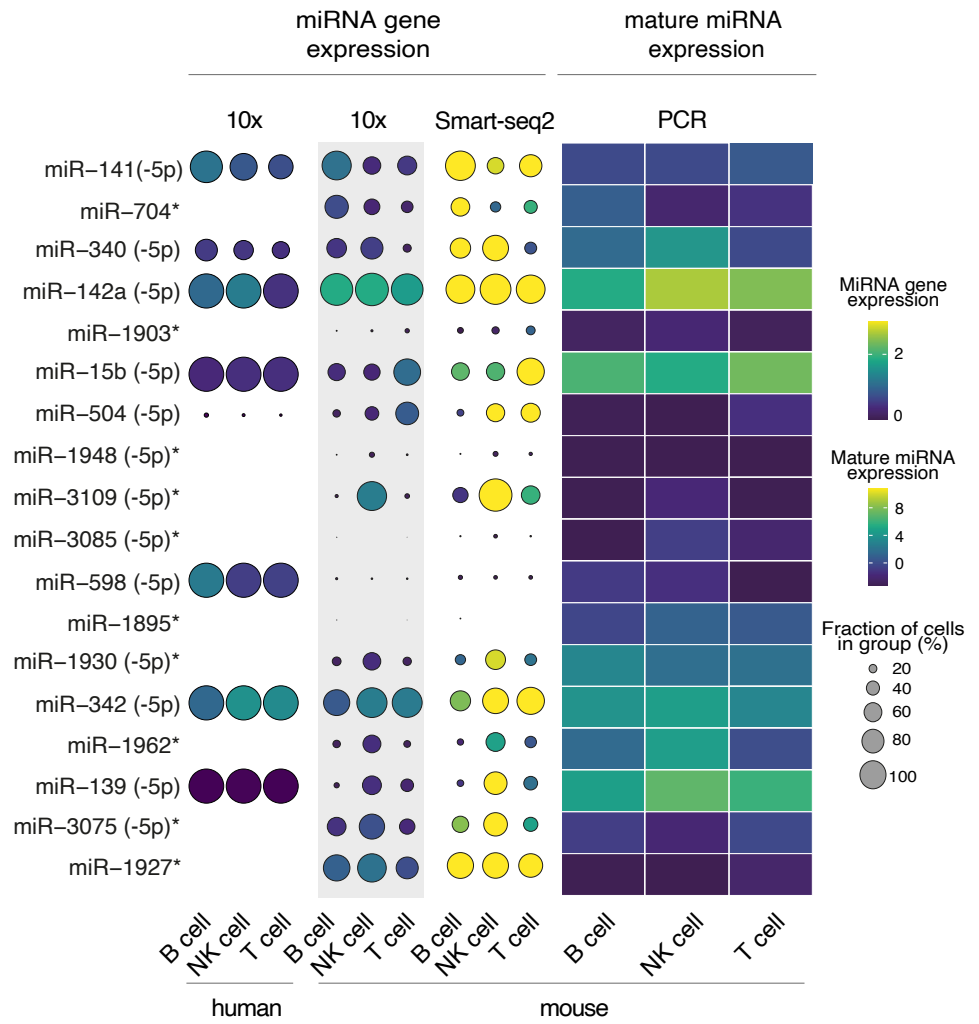
- 884 75. Wolter, J. M., Kotagama, K., Pierre-Bez, A. C., Firago, M. & Mangone, M. 3'LIFE: a functional
885 assay to detect miRNA targets in high-throughput. *Nucleic Acids Res.* **42**, e132 (2014).
- 886 76. O'Leary, N. A. *et al.* Reference sequence (RefSeq) database at NCBI: current status, taxonomic
887 expansion, and functional annotation. *Nucleic Acids Res.* **44**, D733–D745 (2016).
- 888 77. Frankish, A. *et al.* GENCODE 2021. *Nucleic Acids Res.* **49**, D916–D923 (2021).
- 889 78. Kuhn, R. M., Haussler, D. & Kent, W. J. The UCSC genome browser and associated tools. *Brief.*
890 *Bioinformatics* **14**, 144–161 (2013).
- 891 79. Zheng, G. X. Y. *et al.* Massively parallel digital transcriptional profiling of single cells. *Nature*
892 *Communications* **8**, 14049 (2017).
- 893 80. Liao, Y., Smyth, G. K. & Shi, W. The R package Rsubread is easier, faster, cheaper and better for
894 alignment and quantification of RNA sequencing reads. *Nucleic Acids Res.* **47**, e47 (2019).
- 895 81. Farese, R. V. *et al.* Phenotypic analysis of mice expressing exclusively apolipoprotein B48 or
896 apolipoprotein B100. *Proc. Natl. Acad. Sci. U.S.A.* **93**, 6393–6398 (1996).
- 897 82. Powell-Braxton, L. *et al.* A mouse model of human familial hypercholesterolemia: Markedly
898 elevated low density lipoprotein cholesterol levels and severe atherosclerosis on a low-fat chow
899 diet. *Nat. Med.* **4**, 934–938 (1998).
- 900 83. Durinck, S. *et al.* BioMart and Bioconductor: a powerful link between biological databases and
901 microarray data analysis. *Bioinformatics* **21**, 3439–3440 (2005).
- 902 84. Durinck, S., Spellman, P. T., Birney, E. & Huber, W. Mapping identifiers for the integration of
903 genomic datasets with the R/Bioconductor package biomaRt. *Nat. Protoc.* **4**, 1184–1191 (2009).
- 904 85. Mulè, M. P., Martins, A. J. & Tsang, J. S. Normalizing and denoising protein expression data from
905 droplet-based single cell profiling. *Nature Communications* **13**, 2099 (2022).
- 906 86. Korthauer, K. D. *et al.* A statistical approach for identifying differential distributions in single-cell
907 RNA-seq experiments. *Genome Biol.* **17**, 222 (2016).
- 908 87. Mehtonen, J. *et al.* Single cell characterization of B-lymphoid differentiation and leukemic cell
909 states during chemotherapy in ETV6-RUNX1-positive pediatric leukemia identifies drug-
910 targetable transcription factor activities. *Genome Med.* **12**, 99 (2020).
- 911 88. Satija, R., Farrell, J. A., Gennert, D., Schier, A. F. & Regev, A. Spatial reconstruction of single-cell
912 gene expression data. *Nature Biotechnology* **33**, 495–502 (2015).

- 913 89. Wolf, F. A., Angerer, P. & Theis, F. J. SCANPY: large-scale single-cell gene expression data
914 analysis. *Genome Biology* **19**, 15 (2018).
915

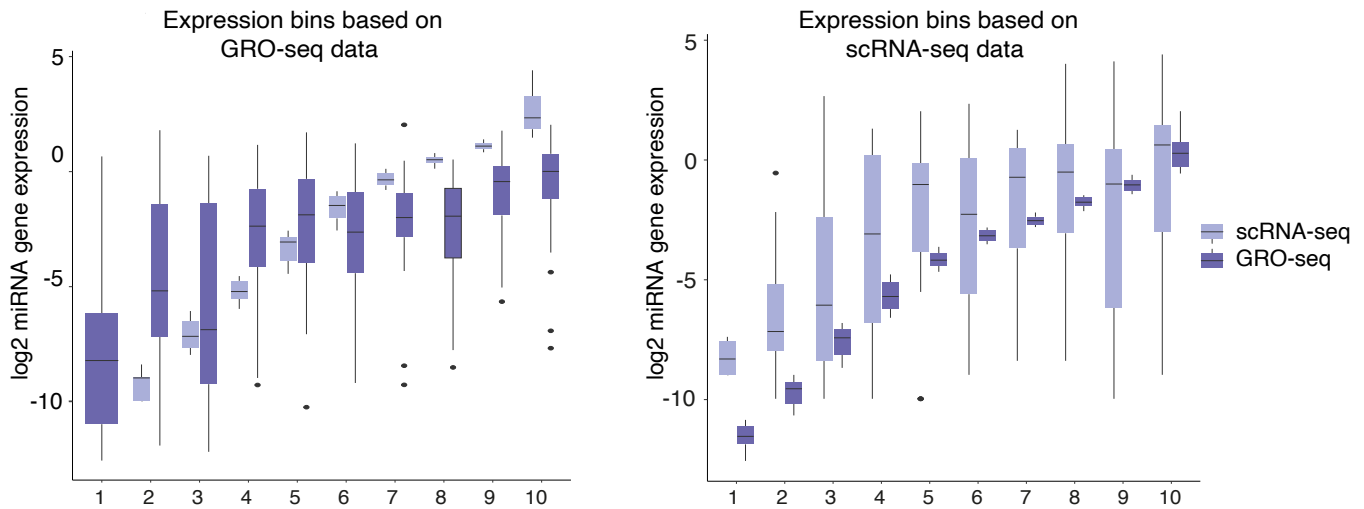
A



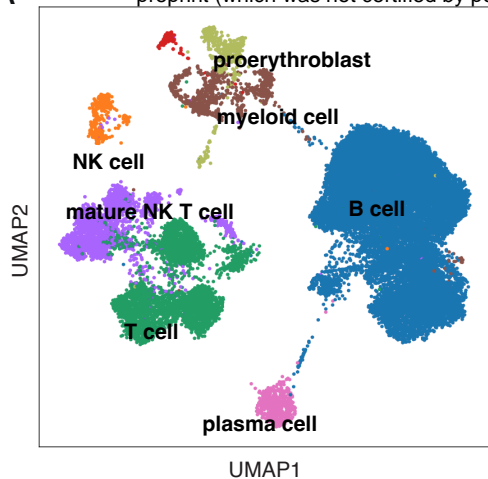
B



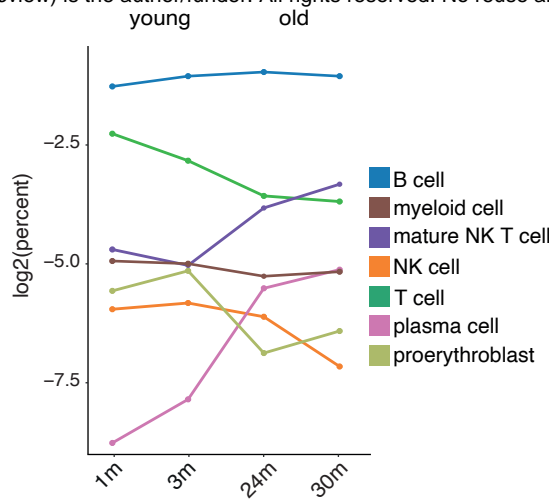
C



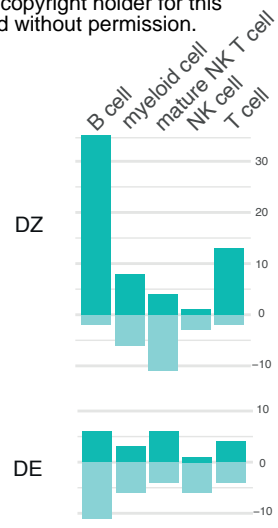
A



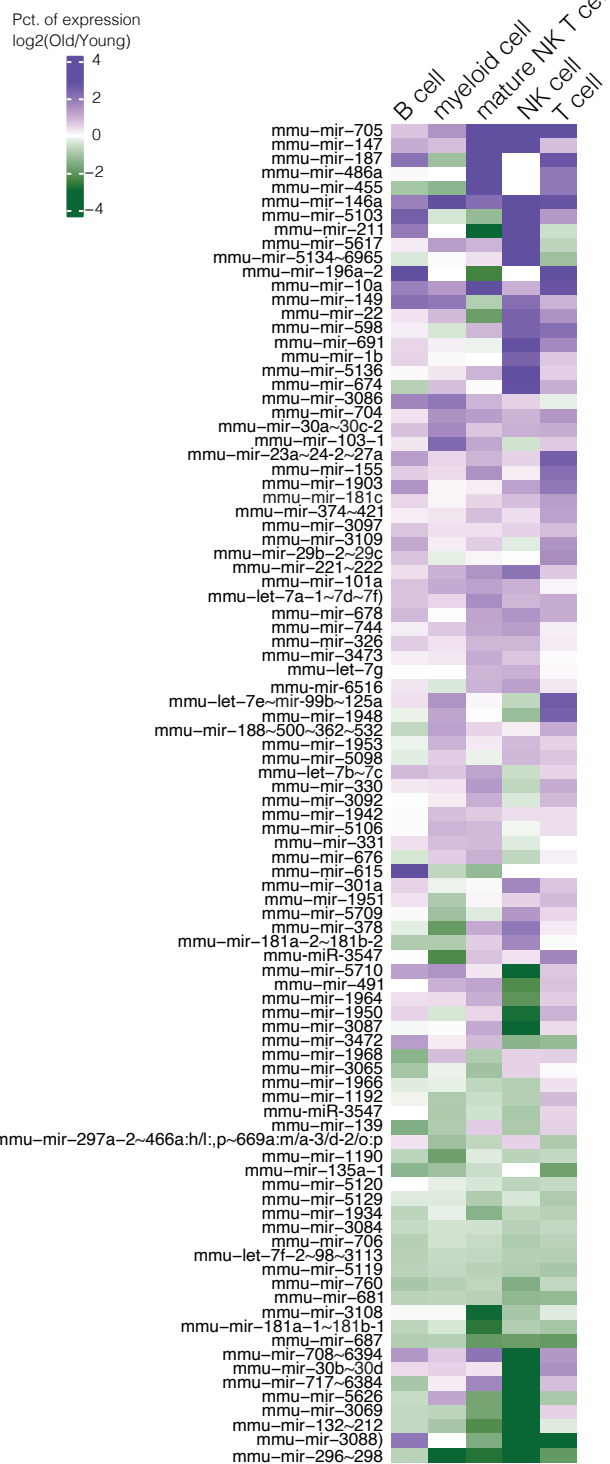
B



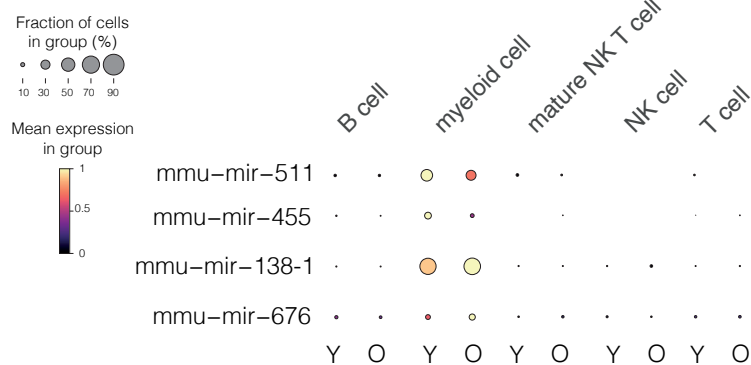
C



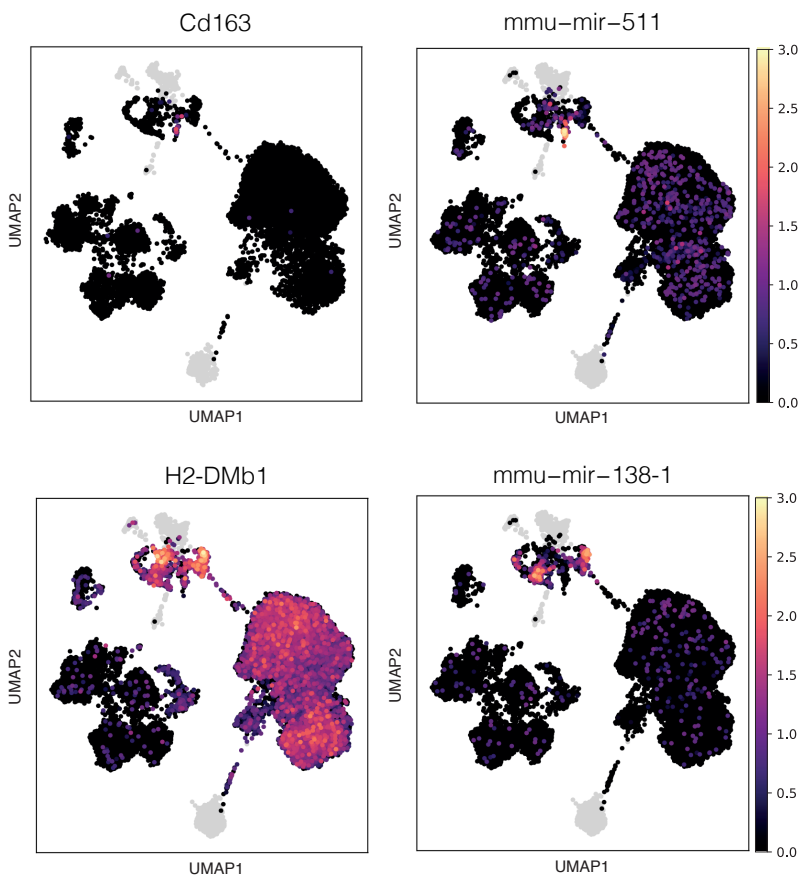
D



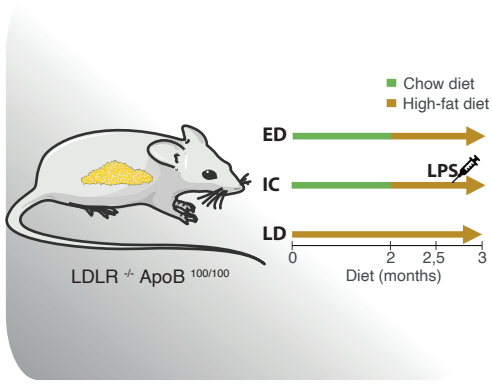
E



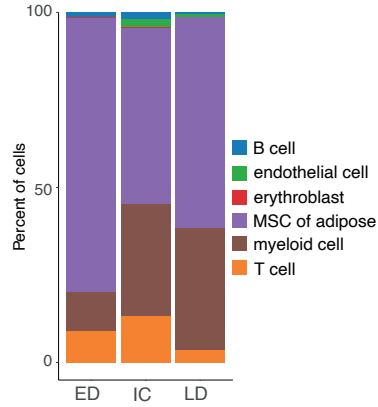
F



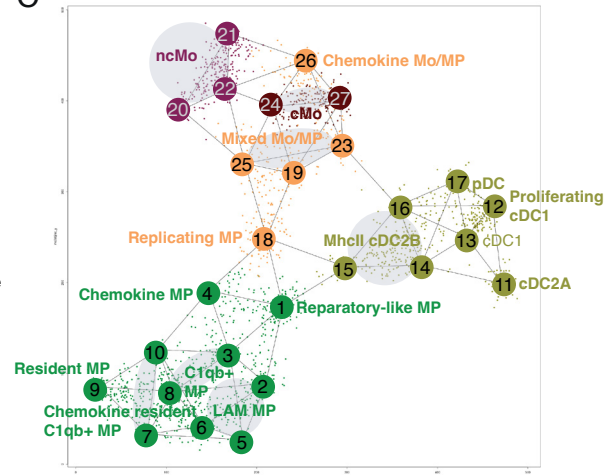
A



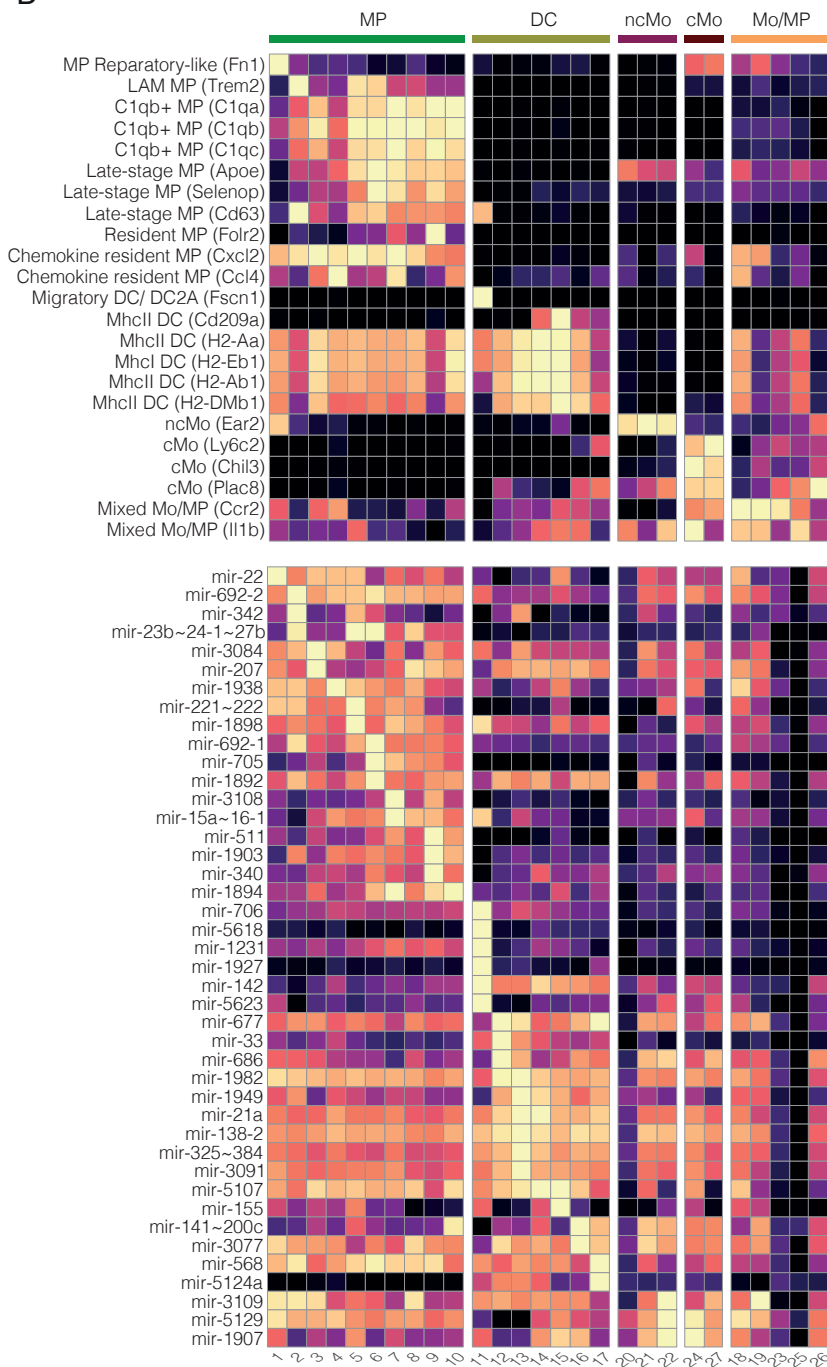
B



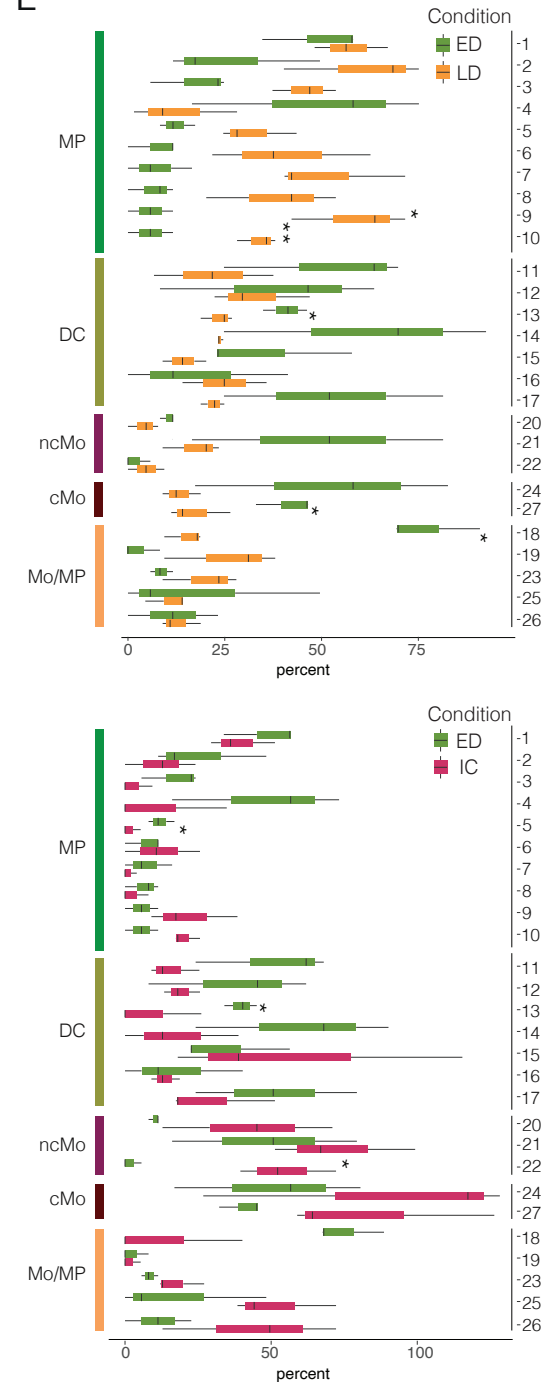
C

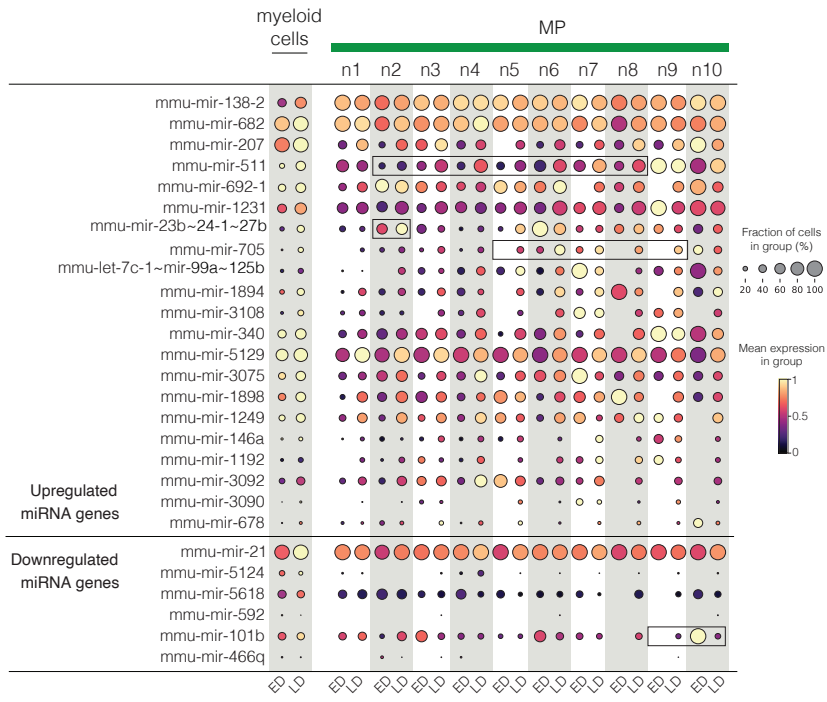


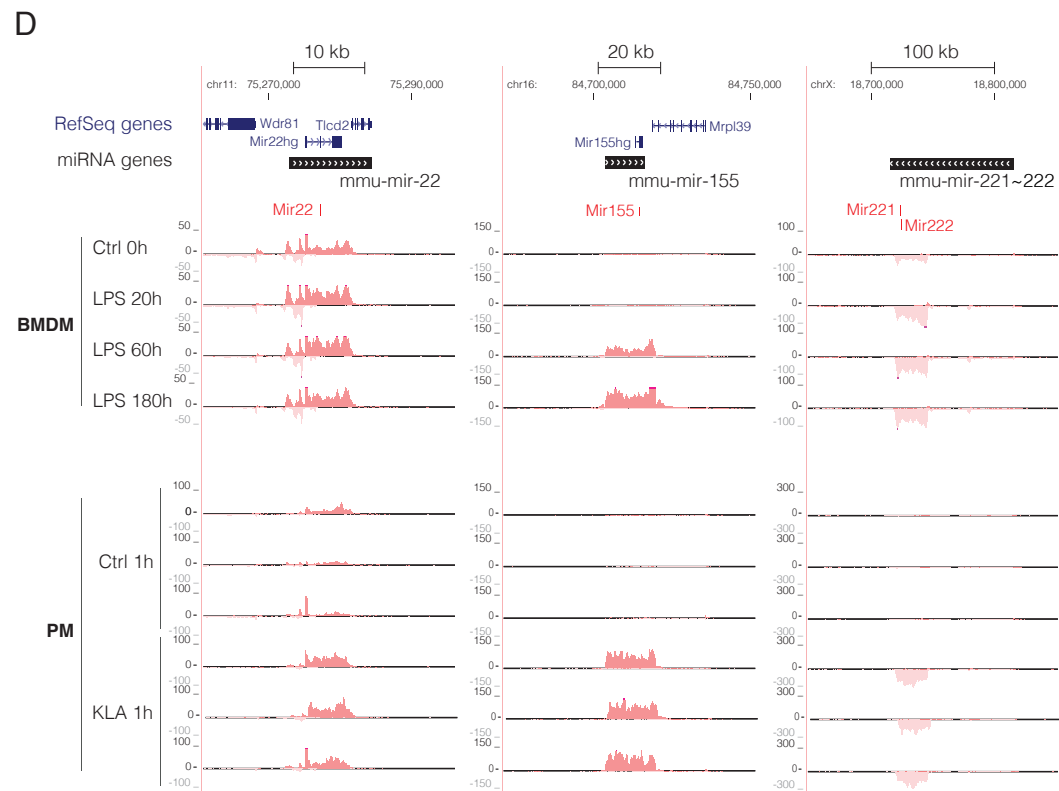
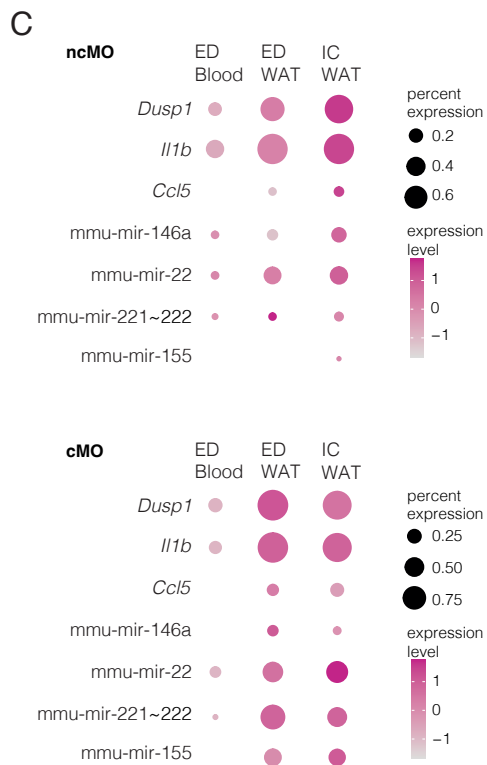
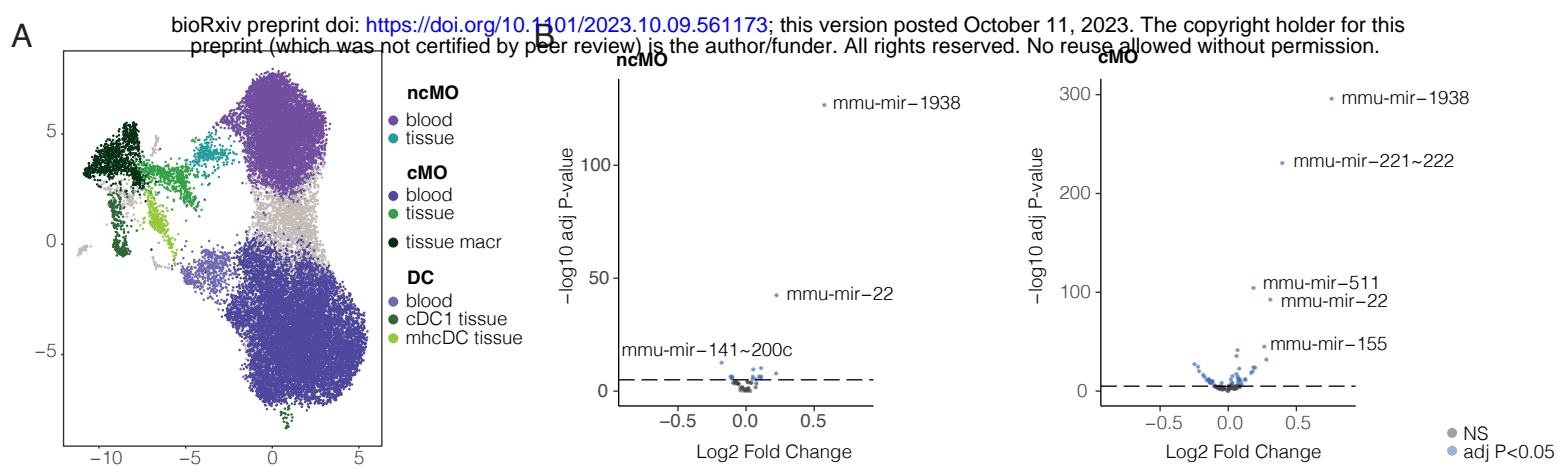
D



E







Supplementary information

Cell-type-specific characterization of miRNA gene dynamics in immune cell subpopulations during aging and atherosclerosis disease development at single-cell resolution

Ana Hernández de Sande¹, Tanja Turunen¹, Maria-Bouvy Liivrand^{1,2}, Tiit Örd³, Senthil Palani⁴, Celia Tundidor-Centeno¹, Heidi Liljenbäck^{4,5}, Jenni Virta⁴, Olli-Pekka Smålander², Lasse Sinkkonen⁶, Thomas Sauter⁶, Anne Roivainen^{4,5,7}, Tapio Lönnberg^{7,8}, Minna U Kaikkonen³ and Merja Heinäniemi¹

¹ School of Medicine, University of Eastern Finland, Kuopio, North-Savo 70200, Finland

² Department of Chemistry and Biotechnology, Tallinn University of Technology, Tallinn 12616, Estonia

³ A. I. Virtanen Institute, University of Eastern Finland, Kuopio, North-Savo 70200, Finland

⁴ Turku PET Centre, University of Turku and Turku University Hospital, FI-20520 Turku, Finland

⁵ Turku Center for Disease Modeling, University of Turku, FI-20520 Turku, Finland

⁶ Department of Life Science and Medicine (DLSM), University of Luxembourg, 4362 Belvaux, Luxembourg

⁷ InFLAMES Research Flagship Center, University of Turku, FI-20520 Turku, Finland

⁸ Turku Bioscience Centre, University of Turku and Åbo Akademi University, FI-20520 Turku, Finland

Table of contents

Supplementary table legends 1-5

Supplementary figures S1-S5 and their legends

Table S1. miRNA gene coordinates and related NGS dataset accession codes

(A) The datasets used for defining genomic intervals for miRNA gene custom quantification and (B-C) 'miRNA gene coordinates' in mm10 and hg19 genomes. Related to Fig. 1. (D-E) 'Dataset accession codes' for 10x and SMART-seq2 'scRNA data used in this study. NCBI GEO accession codes are listed.

Table S2. Spleen scRNAseq summary of differential gene expression across immune cell types analyzed

Differential distribution analysis summary from comparison of old vs young male mice. The statistics for differential detection rate (DZ) (A) and expression level (DE) (C) of miRNA genes are provided separately for each cell type. Includes also ranking of miRNA based on Fisher test combined p-values across cell types (B and D for DZ and DE categories). Related to Fig. 2.

Table S3. Atherosclerosis mouse model scRNA-seq data pre-processing settings and marker genes of WAT myeloid sub-populations

(A) Marker protein-coding and miRNA genes for metanodes defined from myeloid sub-populations in WAT are listed. Related to Fig. 3. (B) Cut-off parameters used in quality filtering of scRNA-seq data collected from LDLR^{-/-}ApoB^{100/100} mice.

Table S4. WAT scRNAseq summary of differential gene expression in myeloid cells at late disease

Differential distribution analysis summary from comparison of late disease vs early disease in LDLR^{-/-}ApoB^{100/100} mice. The statistics for differential detection rate (DZ) (A) and expression level (DE) (B) are provided for myeloid cell comparison of miRNA genes. Related to Fig. 4.

Table S5. WAT and blood myeloid cell scRNAseq and GRO-seq summary of differential gene expression

Differential distribution analysis summary from comparison of tissue vs blood monocyte and monocyte-derived cell populations in LDLR^{-/-}ApoB^{100/100} mice. The statistics for differential detection rate (DZ)(A) and expression level (DE)(B) are provided for miRNA genes. GRO-seq: DE analysis of ex vivo cultured bone marrow-derived CD14+ or peritoneal macrophage stimulated with pro-inflammatory LPS or KLA treatments. Related to Fig. 5.

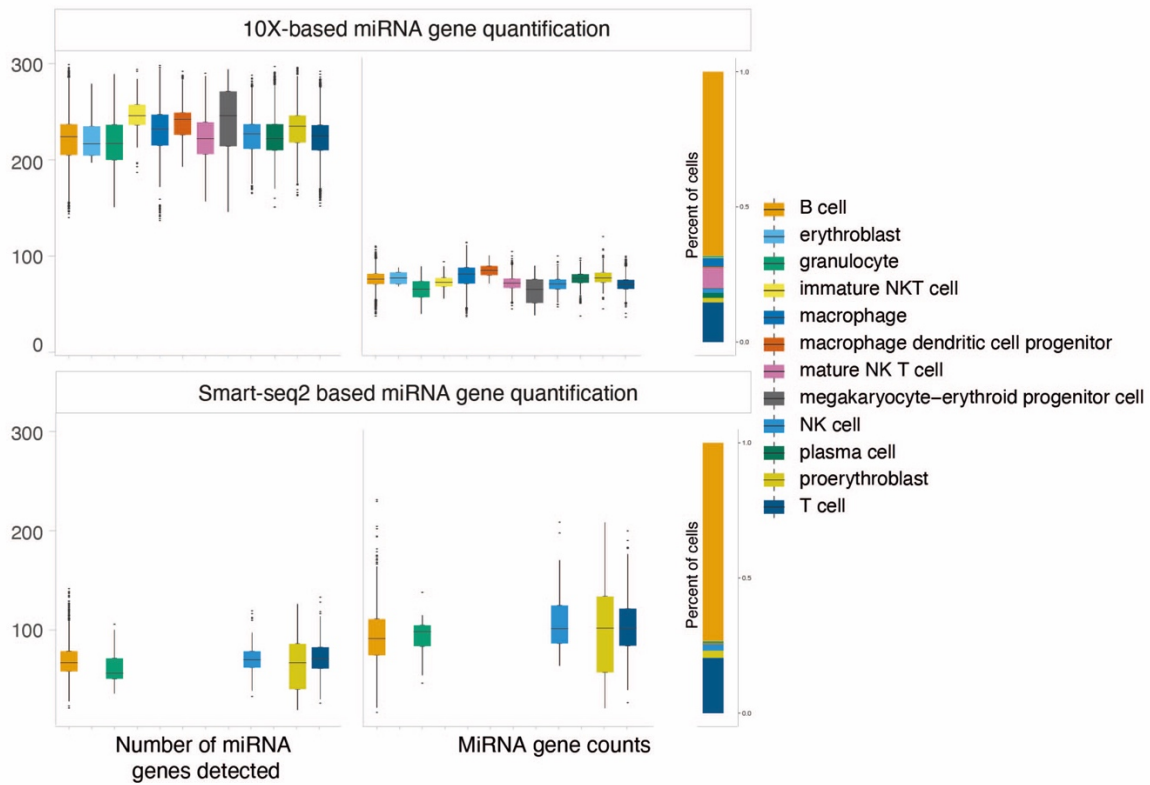


Figure S1. Comparison of miRNA gene expression measured from 10x Genomics and Smart-seq2 scRNA-seq technologies. MiRNA gene detection was evaluated in each splenic cell type by measuring the number of miRNA genes detected and their expression levels in 10x Genomics (upper panel) and Smart-seq2 technologies (lower panel).

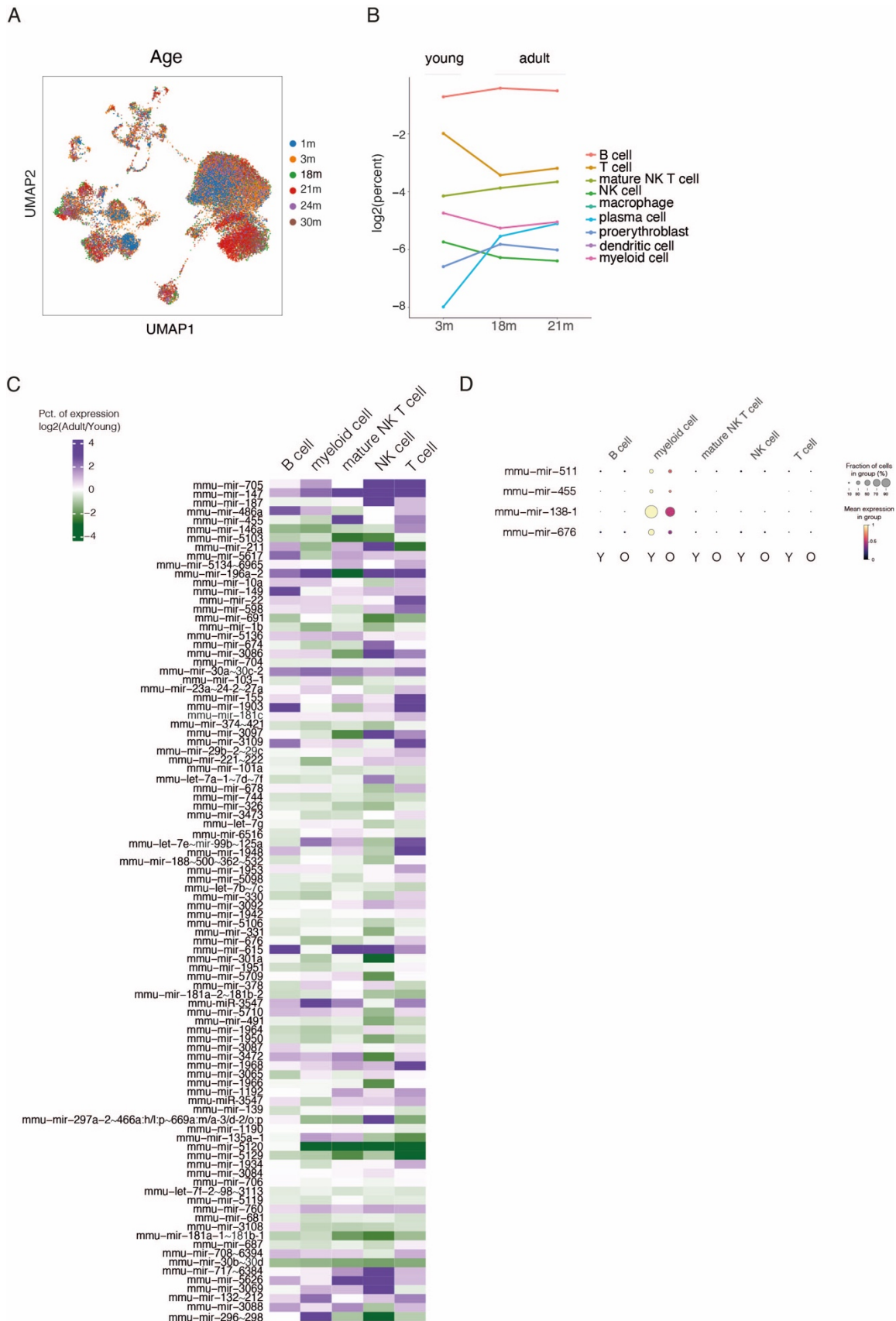
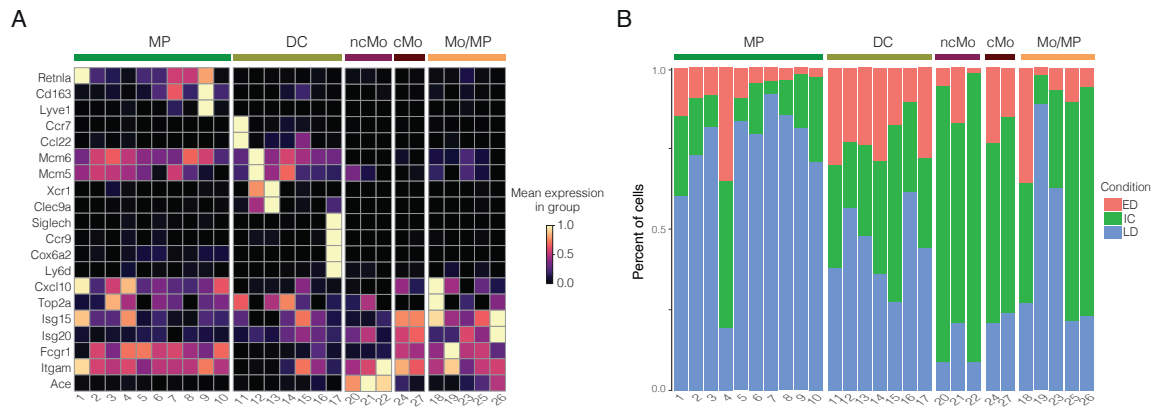


Figure S2. Female analysis of splenic cell types in TMS data. (A) UMAP of spleen tissue colored by age. (B) Cell type percentages from female mice present in each age group of the dataset are shown as a line plot. (C and D) Heatmap of miRNAs found concordantly regulated in splenic male samples during aging and plotted from female samples comprising young (3 months) and adult (18 and 21 months) mice.



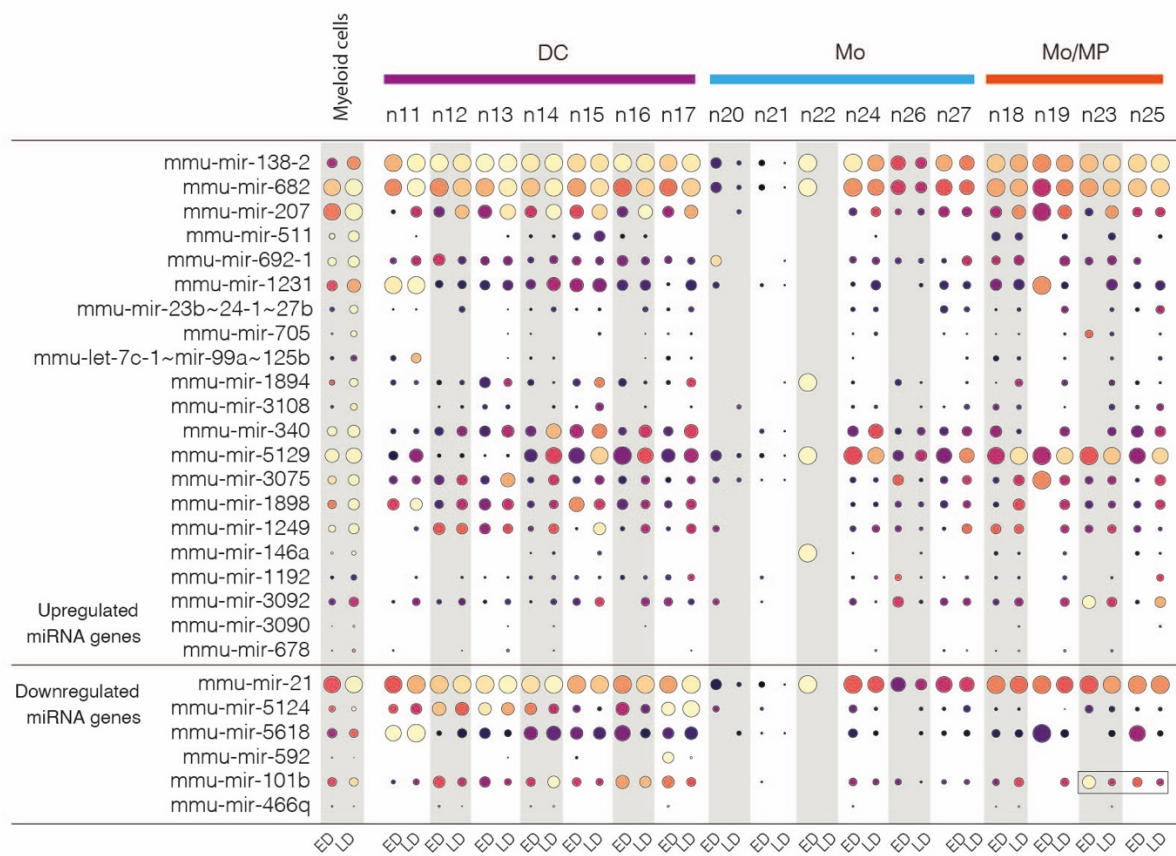


Figure S4. Changes in miRNA gene expression during disease progression in dendritic cells and monocytes. MiRNA genes with altered expression during disease progression are shown as in Fig. 4.

